

Review

Correlating critical current density, quench protection, relaxation time and entropy in superconductors after disturbances—Intermediate summary

Harald Reiss

Department of Physics, University of Wuerzburg, D-97074 Wuerzburg, Germany; harald.reiss@physik.uni-wuerzburg.de

CITATION

Reiss H. Correlating critical current density, quench protection, relaxation time and entropy in superconductors after disturbances—Intermediate summary. *Mathematics and Systems Science*. 2024; 2(1): 2510.
<https://doi.org/10.54517/mss.v2i1.2510>

ARTICLE INFO

Received: 23 January 2024
Accepted: 4 March 2024
Available online: 30 March 2024

COPYRIGHT



Copyright © 2024 by author(s).
Mathematics and Systems Science is published by Asia Pacific Academy of Science Pte. Ltd. This work is licensed under the Creative Commons Attribution (CC BY) license.
<https://creativecommons.org/licenses/by/4.0/>

Abstract: This paper summarizes results recently obtained from simulation of transient temperature excursions in filamentary and thin film superconductors. Under multi-component heat transfer in the complicated conductor cross sections and materials composition of present High Temperature Superconductors, numerical, Finite Element and Monte Carlo simulations are applied to solve Fourier's differential equation with high spatial and temporal resolution. The overall aim was to encircle the quench problem in superconductors and to provide new stability criteria from correlations between superconductor critical current density, density of electron pairs, and relaxation time and entropy. Relaxation, correlation and entropy analysis presented in this paper extends the spectrum of standard methods to avoid quench to a new tool. As results, quench starts always locally, and as a highlight of this investigation, a second "critical" temperature, T_{Quench} , has been identified that with high probability exists below standard critical temperature. Entropy is the driving force for relaxation of the superconductor to new equilibrium after a disturbance.

Keywords: superconductor phase transition; multi-physics; critical current density; quench; relaxation; entropy; convergence; correlations

1. Introduction

Energy levels and their occupation by electrons in superconductors are differentiated by ground and excitation states, like in other solids (**Figure 1**). Excitations of the many-particle, superconductor electron system, which means disturbances of its thermodynamic equilibrium, may result from absorption of radiation, from electron injection or from the frequently neglected, "flux flow"-loss mechanism, see Chap.7 in the study of Huebener [1]. This loss mechanism exists, even below critical temperature, T_{Crit} , when the superconductor, if charged by a large transport current, is exposed to a magnetic field (see later for explanation). Disturbances in superconductors trivially arise also from insufficient or break-down of the cooling system. Even any increase of temperature can be considered a disturbance.

Disturbances, when they cause increase of local temperature, $T(x, y, t)$, not necessarily proceed at constant or at uniform rates in the conductor cross section.

The energy gap, ΔE , the light-yellow shaded area in **Figure 1(a)**, separates ground state from excited electron states. Existence of the energy gap results from quantum-mechanical selection rules. A very small part of the total number of electrons is coupled to electron pairs. Width of the energy gap depends on temperature, T , and decreases with increasing temperature, $T < T_{Crit}$.

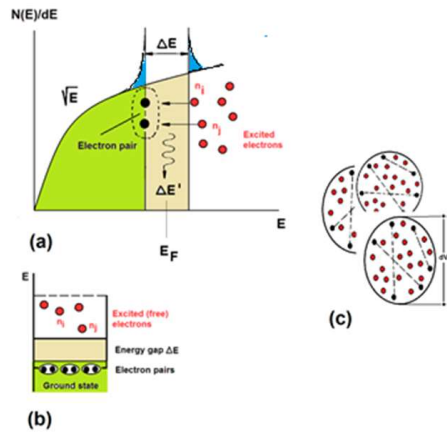


Figure 1. Electron state diagrams in a superconductor.

Figure 1 shows energy states of the disturbed electron system and describes decay of excited electron states (recombination to electron pairs) in the superconductor, under conservation of energy and momentum, after end of a thermal disturbance (all diagrams are schematic, not to scale). The figure shows density, $\rho(E) = dN(E)/dE$, of single particles states (solid curve, proportional to $E^{1/2}$) vs. energy, E , the energy gap, ΔE (yellow shaded area) at the Fermi energy, E_F , the sections (dark-blue) to which electrons from the energy gap are driven (in the literature: “smeared out”), and an escaping phonon of energy $\Delta E'$ of at least $2\Delta E$ to fulfil energy and momentum balance. The dashed curve at E_F around the full circles indicates an electron pair, $(2e)_k$ of a very large number $1 \leq k \leq (N - 1)$ of other pairs $(2e)$. Each shaded, red circle, still in **Figure 1(a)**, denotes an elementary electron excitation. The “source” from which single electrons are selected to condense to pairs consists of (but is not restricted to) the n_i, n_j from the decay of pairs, $(2e)_k$. It is statistically selected following quantum-mechanical principles if conservation of energy (and momentum) can be fulfilled. Far below critical temperature, its number, in dynamic equilibrium, constituting a pair, is a fraction in proportion to $(\Delta E/E_F)^2$ [2] of the number of electrons originally contained in ΔE , a very small percentage of the total electron body. The lower **Figure 1(b)** is included to highlight a very large multiple of electron pairs as being positioned, schematically in this diagram, closely to the lower edge of the energy gap (the top, E_F , of the Fermi Sea); standard interpretation is that all these states are described by a single, coherent wave function, which facilitates simulations. **Figure 1(c)** schematically indicates overlapping coherence volumes (V_C , large circles) with their diameter, dV_C , within which electron pairs (solid, black circles, interconnected by dashed lines) and single electrons overlap (solid red circles, the decay products from the previous decay). Also compare Note 3 how decay and relaxation are modelled in this paper, in contrast to the ideas how relaxation has been understood in other publications

Electrons, electron pairs and phonons (excitations of the ionic lattice) are responsible for electrical and thermal transport in superconductors. Below critical temperature, current transport is almost entirely by electron pairs, if other critical parameters (concerning magnetic field, current density) are not exceeded. Electron pairs bypass the electrical resistance of the normal conducting electrons.

An attempt is made in **Figure 2** to schematically explain, in a resistance network, the contributions by electrons, electron pairs, all in parallel to electrical, and by phonons to thermal transport.

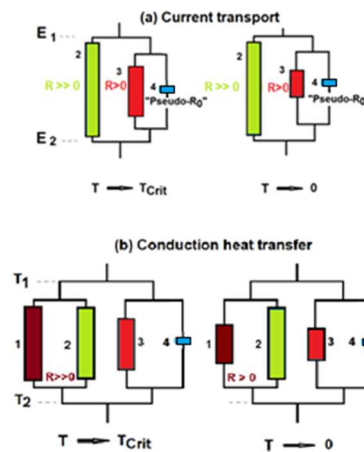


Figure 2. An attempt to explain electrical current transport **(a)** and thermal conduction heat transfer **(b)** in superconductors, the latter by a pseudo-resistance network. In both diagrams, vertical length of the rectangles schematically indicates temperature dependency.

Figure 2(a), above, shows *current transport* at different temperature (schematic, qualitative, and strongly simplified). Numbers 2 to 4 in the rectangles denote: (2) (light-green): Single, not condensed electrons, strongly bound in the Fermi Sea that (without existence of electron pairs) would generate large electrical resistance to current; (3) (dark-red): Excited single electrons or quasi-particles states (both at energy levels above the gap) generating finite, non-zero resistance; (4) (dark-blue): “pseudo-resistance” of electron pairs for application in numerical simulations (in reality: almost zero). The resistance of electron pairs (4) is by orders of magnitudes below the resistance of metals; contribution to current transport through the whole sample therefore is only by electron pairs. In order to design a conduction or resistance model that is applicable for numerical simulations, a “pseudo-resistance” of the electron pairs, at least 20 orders of magnitude smaller value than the resistance of normal (metallic) electrical conduction, was assumed in the calculations. A “phonon rectangle” (1) is omitted in this diagram (the corresponding resistance to current transport would be infinitely large, under standard, low temperature conditions).

Figure 2(b), below, shows *conduction heat transfer* at different temperature (schematic, again qualitative and strongly simplified). (1) (dark-brown, non-zero thermal, phonon resistance, R_{ph}); (2) to (4): thermal resistances generated by items (2) to (4) in the current transport (upper) diagram; the short, dark-blue rectangles in the lower diagram do not indicate vanishing thermal resistivity because electron pairs do not contribute to heat transfer (no collisions with the lattice); a corresponding, thermal pseudo-resistance, R_{∞} , if it existed at all, would have to be treated as “diverging” in the numerical simulations.

At very low temperature, heat transfer is subject to resistances $R_{ph} > R_{EI}$, the thermal conductivity of the superconductor to the most part is by single (not condensed) electrons. The solution of Fourier’s differential equation yields *phonon* temperature, that at any co-ordinate, and if relaxation is not completed, is different from electron temperature in resistances 2 and 3, in particular if coupling between electrons and lattice is weak. Temperature of rectangle 3 like rectangles 1, 2 and 4, is below T_{Crit} (approaches equilibrium temperature after a disturbance when relaxation is completed).

1.1. Relaxation in superconductors

Excitations in superconductors increase occupation of electron energy levels above ΔE . The reverse process, relaxation of excited electrons to electron pairs and to a new dynamic equilibrium, involves correlations among excited electrons with those below the energy gap.

Relaxation needs time. Calculation of relaxation time that an excited superconductor needs to relax to a new thermodynamic equilibrium hardly ever has been investigated in the superconductor literature. But impacts of relaxation and relaxation time on critical current density, J_{Crit} (because of its strong dependence on temperature), and also impacts on all those observables that depend on critical current density (like levitation height of a sample in magnetic field, or distribution of shielding or transport currents), are too important to be neglected. A method to estimate relaxation time will be explained in this paper.

How to obtain relaxation time in normal conductors (metals) has been reported in the literature; a particular method will be referenced in part B, Sect. 6.2, of this paper. But the method assumes diffusion processes and energy exchange proportional to the temperature difference between electrons and lattice ions. This is not applicable in presence of electron pairs in superconductors.

In strong contrast, electron pairs in superconductors do not feel electrical resistance since they would be typical for diffusion processes. There is no unprofitable diffusion of electron pairs across classical resistive obstacles.

The present paper revisits a recently suggested method to calculate relaxation rates and relaxation time. The paper investigates how and to which extent entropy production during the relaxation process is important for stability of superconductors against quench. Entropy yields the answer why excited electron states at all should relax to recover from disturbances to a new thermodynamic equilibrium and to superconductor stability.

A superconductor is stable if it does not quench, during or after a disturbance. During quench, electromagnetic energy stored in a magnetic field may suddenly be released from the superconductor volume. This very quickly raises superconductor temperature and may lead to its destruction.

Quench can be avoided by application of stability models to design, manufacture and operation of superconductor devices.

Standard stability models [3–5] essentially are stationary energy balances, frequently applied assuming worst case conditions. But quench, as a short-time, and as we will see, a multi-physics problem in highly diversified, superconductor cable cross sections, cannot adequately be analysed by stationary energy balances.

As a step forward, numerical simulations have been suggested by the present author [6–9]. The simulations have demonstrated that after disturbances, the temperature fields in filamentary and in thin film superconductors not only are transient but also non-uniform, $T = T(x, y, t)$, contrary to the simplified assumption, $T = T(t)$. The latter is the traditional view. It has been applied not only in the special case of standard stability models but can be found also in the overwhelming, general part of traditional superconductor literature.

Contrary to the traditional view, local temperature variations, in case there are local heat sources in the conductor cross section, may amount to 4 K between four nodes of a small, materials volume element which means, within a rectangle of just $2 \mu\text{m} \times 30 \mu\text{m}$, the size of a single plane, 4-node element in a Finite Element simulation scheme of a thin

film superconductor. Likewise, temperature variations, in the order of up to 10^6 K/s, may arise under disturbances.

This prediction has far-reaching consequences: When the simulated, transient temperature fields are mapped onto the field of critical current density, J_{Crit} , also J_{Crit} , becomes non-uniform and transient, $J_{Crit} = J_{Crit} [T(x, y, t)]$. Traditionally, J_{Crit} is a unique function of temperature (injective in the mathematical sense), $J_{Crit}(T) = J_{Crit0} (1 - T/T_{Crit})^n$, with J_{Crit0} a constant and the exponent n of about 0.5 (see later for tests made using different values of n).

Non-uniformity of $T(x, y, t)$ and, as the consequence, also of $J_{Crit}(x, y, t)$, in type II superconductors, e. g. by the flux flow mechanism, may cause the material to locally become “flux flow”-resistive, in the first instances during or after a disturbance¹. Impacts of this disturbance on conductor temperature is significant, as can be seen by inspection of transient temperature excursions when flux flow losses quickly raise conductor temperature to values above T_{Crit} , which means create also Ohmic resistive states. See later, the excursion with time of temperature in part B of the paper. Flux flow losses invariably lead to a quench if no measures can be taken to instantaneously distribute the losses, within the material or to a coolant, or to interrupt transport current.

Superconductor temperature, and flux flow, Ohmic resistance and quench, all to be uniformly distributed and obtained simultaneously in the whole conductor cross section (and volume), would request uniform materials properties, and in case of a single, isolated disturbance, infinitely large, thermal transport properties of the superconductor material. These conditions are fulfilled neither in superconductors, not in any realistic solid material. Therefore, quench in superconductors, too, will not occur uniformly and simultaneously in the total conductor cross section. Contrary to standard assumptions, quench always starts locally.

This process, the distribution of hot spots and local quench, can be analysed by numerical calculations with high spatial and temporal resolution [6–9]. But numerical solution of temperature excursion, energy balances and of the quench process is not the end of investigating superconductor stability.

In a superconductor, we have a variety of different particle and quasi-particle sets (including excitation of the lattice if one imagines also contributions from wave/particle dualisms). All these sets determine distribution of local temperature, of critical current density, resistances, magnetic field penetration and distribution of transport current. For the special case of electrical current transport and of internal heat transfer, a minimum of sets is listed below that has to be taken into account in stability analysis².

Each of these sets obeys different transport, decay and interaction rules. The wave/particle dualism, for example, enables radiative transfer to be treated as a particle flow in Monte Carlo simulations of the distribution of photons and their absorption/remission, while temperature fields result from solution of Fourier’s differential equation, a continuum theory.

This means, if we wish to improve understanding the physics behind quench, and how to avoid quench, a new holistic, multi-physics approach is needed to complete the solution of the stability problem.

Stability against quench has frequently, and honestly speaking, quite successfully been discussed in the literature though under engineering aspects only. Analysis and solution of the quench problem by engineering aspects has successfully been demonstrated also in practice (with painful exceptions, however). In contrast, the numerical approach presented in this paper has to integrate superconductor relaxation,

which means a description of origin and, most importantly, lifetime of disturbed states (the relaxation time). This is because the number N_{Eq} of electron pairs necessary to provide zero-loss current transport under equilibrium conditions is subject to lifetime of disturbances and of disturbed states during which the number N_{Eq} might become too small.

The literature describes no efficient method to calculate relaxation time in superconductors. We find only more or less inappropriate (Sect. 6), sometimes even questionable explanations. Let us consider the following:

Buckel and Kleiner [10], 1st paragraph, explain “In conventional superconductors, with decreasing temperature the concentration of unpaired electrons decreases exponentially. Hence, the probability that an unpaired electron finds a suitable partner for the recombination to form a Cooper pair also decreases” end of this citation³.

Likewise, investigating the time-dependence of the decay of trapped magnetic flux is frequently realized by means of considering the time dependence of magnetisation, $M \sim t^{-\alpha}$, of a sample, but this, too, does not provide a systematic model, and reported results usually provide just fit to experimental data.

As a step forward, a “Microscopic Stability (relaxation) Model” [11] has been suggested previously. A first application of this model was reported in Reiss [12]. As a corollary, the present paper revisits this model to investigate a possible existing second critical temperature below the traditional one, and of correlations between critical current density, J_{Crit} , relaxation time and entropy production.

Dynamic equilibrium, the electron state obtained after completion of the relaxation process, is achieved after a multiple of discrete sequential [11], “repair” (i.e. relaxation) steps. A minimum number of electron pairs are necessary to provide zero-loss current transport. The question is whether this minimum number safely can be determined in view of the strongly temperature dependent critical current density. We will see later that calculation of “stability functions” provides an instrument helpful for solution of this problem.

As an example, how relaxation time becomes important, a levitation experiment shall be mentioned. A non-zero, stable levitation height, Z , is obtained only if the Meissner effect is established in a large (a minimum) part of the total conductor volume when a superconductor pellet is exposed to magnetic field, and this process can be completed within the period τ , the relaxation time.

Focus of the Microscopic Stability Model [11] thus is on calculation of relaxation time, τ , and of relaxation rates of the disturbed electron system.

1.2. Organization of the paper

The paper is divided into parts A to B: We first concentrate on general issues of the superconductor stability problem and its consequences.

Part A (**Figures 1–14**) explains that traditional stability problems thoroughly have to be updated, from their solely engineering, analytical methods to numerical simulation of temperature fields in superconductors, with high spatial and temporal resolution. Contrary to traditional understanding of superconductivity, we make an attempt to also demonstrate existence of a second critical temperature; this prediction is tightly related to relaxation of an excited superconductor and is explained as a corollary obtained from the foregoing numerical temperature field calculations. We present a correlation analysis and the investigation because why at all an excited superconductor should relax to a new thermodynamic equilibrium (See the same figures).

Part B of the paper is fully dedicated to description of the multi-physics methods applied for simulation of transient temperature fields, of relaxation time and relaxation rates and their consequences for zero-loss current transport. Emphasis is laid on the radiative contribution, how it can be included in parallel to conductive heat transfer and how serious numerical convergence problems have been solved and the solution was confirmed. Encircling the local origin of a quench is successfully demonstrated by the new, numerical method, a result that cannot be obtained with traditional stability models.

Finally, experiments are suggested to check whether the predictions made in part A and B can be verified (Sect. 7).

2. The suggested “Microscopic Stability Model”

The overall concept of the model, with a description of its details and some first applications, has been explained by Reiss [11,12] and will not be repeated here. The following is a short overview:

Focus of the model is on decay of electron pairs under temperature increase, and the reversal process, i.e. re-condensation of the decay products to pairs in a new dynamic equilibrium⁴.

By a very large number of single, successively performed “repair” (relaxation) steps each of which takes the electron system a time interval, ∂t , in the order of 10^{-14} s, the time to obtain the new dynamic equilibrium is calculated by summation of these microscopic time intervals to total relaxation time, τ . The large number of individual relaxation steps results from the number M of individual electrons taken from the whole electron body (indicated by the shaded light-green and dark-blue sections in **Figure 1(a)**), not only of the previously excited ones, N (for specification of M and N compare again Note 3). The individual ∂t in the present paper is calculated from analogies to nuclear physics (exchange Boson, Yukawa interaction, and the “time of flight”-concept)⁵.

The model applies a multi-physics approach using analogies between relaxation in superconductors with re-organisation of the occupation of nuclear energy states, theory of heat transfer, in case of thin films or filaments not only by solid conduction but also, and in parallel, by radiation heat transfer. The calculations apply solutions of the Equation of Radiative Transfer and of the Equation of Conservation of Energy, see later, Equations (12) and (13), of which diffusion approximations, all assisted by application of the Monte Carlo method, are very helpful. Besides, the model applies statistical methods to cover deficiencies (random deviations from perfect, uniform materials properties) that may arise during manufacture, handling (winding) and practical application of these materials in energy technology (cables, transformers, current limiters).

Once relaxation time is obtained [11] from these calculations, the question then is whether relaxation rates in superconductors, possibly under accelerated thermal run-away, are large enough to successfully re-organize the decay products to the new dynamic equilibrium of the electron system, in due time before quench, finally in the whole conductor cross section, becomes inevitable.

“In due time” means: Relaxation rates must be large enough to complete the total relaxation process (to zero loss current transport) within the relaxation time and before another disturbance might arise that possibly would push the superconductor beyond a critical excitation state (a possibly existing “state of no return”), an item that will be addressed in Sect. 3.

At temperature clearly below critical temperature, $T \ll T_{Crit}$, time to complete relaxation is expected, and will be shown below, to be so small that it hardly can be seen in standard experiments. But relaxation time may strongly diverge if T closely approaches T_{Crit} . Compare again Note 3, experiments to determine relaxation time are suggested in Sect. 7 of the present paper.

Other methods to calculate relaxation time and relaxation rates, alternative to the study [11], might exist or be found in future. But relaxation time obtained from any model reasonably would be non-zero and, like found in the study [11], should strongly increase when approaching the superconducting/normal conducting phase transition.

The numerical, Finite Element simulations using the model [11] have been applied to the “first generation” (1G), multi-filamentary BSCCO 2223, and to the (2G) thin film, coated, multi-layer YBaCuO 123 superconductors. Shorthand notations like BSCCO 2223 and YBaCuO 123 are frequently used in the literature, for $\text{Bi}_2\text{Sr}_2\text{Ca}_2\text{Cu}_3\text{O}_{10}$ and $\text{YBa}_2\text{Cu}_3\text{O}_7$, respectively, some with indication also of oxygen deficiency. Both conductors are addressed as “High Temperature Superconductors, HTSC, of $T_{Crit} = 108$ (BSCCO 2223) and 92 K (YBaCuO 123)., Presently, the thin film, coated, multi-layer YBaCuO 123 is preferred for industrial applications of superconductivity in energy technology.

Figure 3 shows the cross sections of a first generation (1 G), multi-filamentary superconductor tape consisting of 91 single filaments of BSCCO 2223 material.

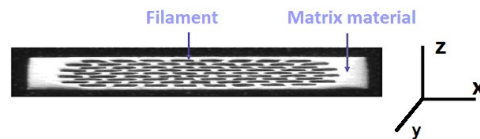


Figure 3. Overall view of the cross section of one tape of the BSCCO 2223/Ag Long Island, multi-filamentary cable (schematic, not to scale). Reprinted from J. Supercond. Novel Magnetism 29 (2016) 1449–1465, Figure 1a.

The number $N = 91$ of identical filaments is in parallel integrated into this tape, and a large number of tapes is switched in parallel to yield total superconductor cross section (10^{-4} m^2). Dimensions of filaments and tape in x (horizontal) and z (vertical) directions are: $x = 280 \mu\text{m}$ (filament) and 3.84 mm (total tape width), and $z = 20 \mu\text{m}$ (one filament) and 264 μm (total tape thickness), respectively.

For a second generation (2G) superconductor, a coil using 100 turns of a multi-layer, thin film coated, YBaCuO 123 superconductor, the cross section of a single turn is shown in **Figure 4**.

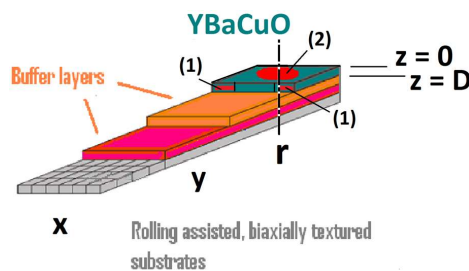


Figure 4. Overall view of a second generation (2G) thin film, coated conductor (schematic, not to scale; geometry and dimensions according to Freyhardt, 2004, lecture notes, apparently unpublished). The Figure is copied from Fig. 6a of [8]. Reprinted from J. Supercond. Novel Magnetism 33 (2020) 3279–3311, Figure 6a.

The vertical, dashed-dotted line denotes the axis of symmetry of the target (the symmetry axis of the target plane ($z = 0$, solid red circle) is perpendicular to the conductor (x, y)-plane. Preferentially, crystallographic c -axis of the YBaCuO material is oriented parallel to the z -axis in this figure, to achieve favourable current transport and solid thermal conduction properties in the YBaCuO film. The target indicates position of local heat sources within the conductor cross section (item 1), or (item 2, the red circle). For the simulations, the heat source is located on the upper surface of the superconductor thin Film. Thickness of the film is $2\ \mu\text{m}$, with its width of $6\ \text{mm}$. Protective coatings (not shown in the figure) serve for thermal/mechanical stabilisation of the conductor and, if necessary, as bias for temporarily taking over transport currents if they exceed critical current of the film, to avoid flux flow losses in a magnetic field. The substrate is prepared by rolling-assisted bi-axial texturing of Ni or Ni-alloys like NiW, NiCr or NiV that are mechanical supported by additional stainless-steel layers soldered on substrate materials. Buffer layers (CeO, YSZ) by epitaxial growth serve for gradual adapting the bi-axial texture from the substrate to the YBaCuO film. The simulation scheme of a coil with 100 windings that applied this conductor will be shown later in part B of the paper. Current transport is almost entirely within the x, z -cross section, i.e., parallel to the (x, y)- (the crystallographic ab -) plane (the crystallographic c -axis of the YBaCuO material accordingly is (anti-) parallel to the z -axis of the co-ordinate system). The target indicates position of sudden, conductive and radiative heat sources. For more details of the composition of this conductor see **Figure 15**.

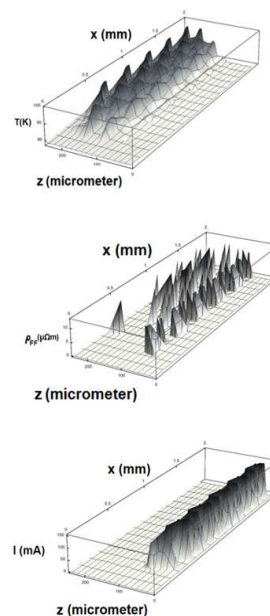


Figure 5. Distribution of conductor temperature (top), flux flow resistivity, ρ_{FF} (below), and of transport (fault) current, I (bottom of the figure), in the x, z -cross section (**Figure 3**) of the multi-filamentary BSCCO 2223 tape, for a low-voltage application. The figure is copied from Fig 5a–5c [6]. Reprinted from J. Supercond. Novel Magnetism 29 (2016) 1449–1465, Figure 5a, b.

Simulated temperature distribution in the (1G) multi-filamentary superconductor are shown in **Figure 5**, with its 3D-plot of $T(x, y, t)$, and in **Figure 6**, the temperature excursion of the centroid element in turn 96 of the thin film, multi-layer superconductor

(results obtained also for filamentary NbTi superconductor have been reported in the study [13]).

In **Figure 5**, only the left half of the cross section, $x \leq 1.92$ mm, $z \leq 264$ μ m, is shown. Results are presented at $t = 8.3$ ms (1.8 ms after start of the disturbance). Flux flow resistivity $\rho_{FF} > 0$ at positions x, y exists only if transport current density at these positions exceeds critical current density, $J_{Transp} > J_{Crit}$, and if local conductor temperature, $T(x, y, t)$, is below local critical temperature. Resistive and zero loss states co-exist in parallel if over-current cannot be compensated, e.g. by switching it to a shunt. Transport current then circumvents resistive transport channels (Ohmic and flux flow). Heat sources in the present case are distributed in the conductor. The distribution of transport current may be different at different length (y-co-ordinates of the tape. Note orientation of the coordinate axes. The number N_{El} of elements in this Finite Element simulation and in one tape is $N_{El} = 4032$.

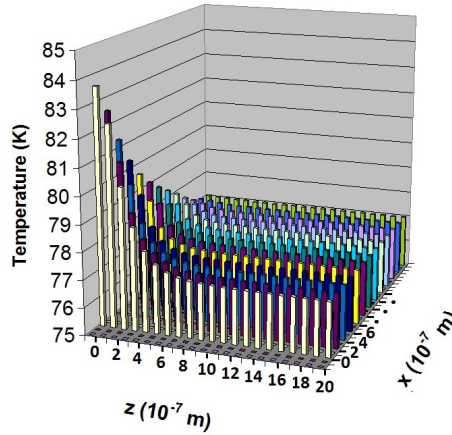


Figure 6. Superconductor temperature distribution (nodal values, at $t = 8$ ns). Reprinted from J. Supercond. Novel Magnetism 33 (2020) 3279–3311, Figure 7.

In **Figure 6**, results are shown at increasing vertical co-ordinates (depth of the YBaCuO 123 thin film explained in the text), z , when a rectangular heat pulse of total $Q = 1.25 \times 10^{-12}$ Ws, is incident on the target ($z = 0$; its position is indicated by the red circle in **Figure 4**). Total duration of the pulse is 8 ns. Penetration depth of the radiation is parallel to the axial direction of its co-ordinate system. The combined Monte Carlo/Finite Element method is applied under the Additive Approximation. In steps of 0.1 μ m, the figure shows temperature between $0 \leq z \leq 2$ μ m and within $0 \leq x \leq 1.2$ μ m (of in total $x \leq 5$ μ m extension in the simulations) of the thin film. The (z -) direction is (anti-) parallel to the crystallographic c -axis of the superconductor material. The figure covers one half of the total x,y -plane and demonstrates anisotropic scattering of incident radiation. The figure is copied from **Figure 3** [8].

How these temperature distributions have been obtained, by which numerical procedures (coupled Monte Carlo and Finite Element calculations, to solve Fourier's differential equation, will be described in part B of this paper.

From the obtained transient conductor temperatures, three very interesting conclusions can be drawn on:

- 1) Prediction of the existence of a second critical temperature.
- 2) Correlation between relaxation time and critical current density.
- 3) Correlation between relaxation time and entropy.

These items are described in the following (Sects. 3 to 5). This is not “new physics” but solely results from interconnection of simulated temperature excursions with traditional physics disciplines.

3. Prediction of a second critical temperature

First, **Figure 7** shows calculated relaxation time for the YBaCuO 123 thin film superconductor. It immediately demonstrates that an additional critical temperature, T_{Quench} , should exist in the superconductor:

The dashed-dotted, horizontal lines in this figure indicate process times (measuring or simulated intervals, δt) during which experiments or simulations are performed. We provisionally assume δt as 50 or 1 μs (justification of these values will be given in Subsects. 3.1 and 3.2). For practical J_{Crit} -measurements, length δt would certainly be larger than these intervals, see later.

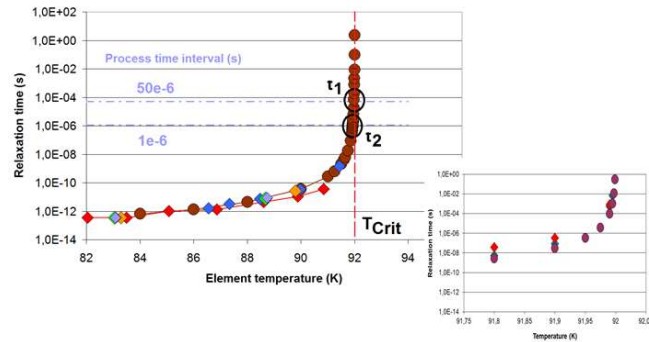


Figure 7. Relaxation times, τ , that the electron system of the YBaCuO 123 superconductor needs to arrive at a new dynamic equilibrium after a disturbance. Reprinted from J. Supercond. Novel Magnetism 31 (2018) 959–979, Figure 8.

Conductor architecture and its materials composition will be shown in **Figure 15**. The disturbance to the most part originates from transport current density locally exceeding critical current density (flux flow resistance). The corresponding flux flow losses steadily increase local conductor which finally may become larger than critical temperature, T_{Crit} , to complete a quench. Results are calculated from the model [11,12] at temperatures in the centroid of turns 96 (light-green, lilac, orange and blue diamonds, respectively) and 100 (red diamonds) of a coil of in total 100 turns. All diamonds indicate relaxation times obtained when using element temperatures resulting from the Finite Element (FE) simulations, while dark-brown circles are calculated for an arbitrary temperature sequence. The dashed-dotted horizontal lines indicate tentatively assumed process times, δt (50 or 1 μs) that intersect (open circles) with the τ -curve (solid, dark-brown circles) at temperatures $T_{1,2}$ of 91.925 or 91.995 K, respectively. As soon as element temperature (experimental or simulated in the FE calculations) exceeds $T_{1,2}$, the corresponding τ are larger, and coupling of all single electrons in this thin film superconductor to a new dynamic equilibrium can no longer be completed within the assumed δt . With modifications (insertion of the relaxation times, $\tau_{1,2}$, in the open, black circles, and the inset to the right), the figure is copied from Fig. 8 [12]. The inset in the present figure shows that if temperature closely approaches T_{Crit} and when using the Fermi distribution function, or a Boltzmann factor (though this violates the condition $E - E_F \gg kT$), or to save computation time, the occupancy number (the probability to

occupy energy levels above the energy gap) even was neglected (curves 1 to 3, respectively), the results obtained for the relaxation time become very close, and again all results diverge.

The large number of decimal points in $T_{l,2}$ of 91.925 or 91.995 K (**Figure 8**) and in particular at $T = 91.99999$ K in the same figure seems to be unphysical. But this solely serves for numerical demonstration of the divergence of relaxation time near the phase transition. This is because the probability F_E , in Note 9 approaches the more closely a constant, while $n_s(T)/n_s(4K)$ diverges (see below, **Figure 9**), the more temperature approaches T_{Crit} .

Existence of T_{Quench} then follows from intersections (open circles) of the horizontal lines with relaxation time, the τ -curve (dark-brown circles). By close inspection of the curves, the points of intersections in this example are identified at temperatures $T_{l,2}$ of 91.925 or 91.995 K, respectively.

As soon as element temperature (experimental or as simulated in simulations) exceeds $T_{l,2}$, the requested relaxation times τ will increase, and coupling of all single electrons to pairs in the investigated thin film superconductor to a new dynamic equilibrium can no longer be completed within the given intervals, δt .

Corresponding to **Figure 7**, density $n_s(T)/n_s(T_0)$, of electron pairs is shown in **Figure 8**, a result obtained with again the model [11] (it has been explained [12] that this ratio is closely related to the Ginzburg-Landau “order parameter” [14]).

Note the strong, diverging decrease of the density of electron pairs in **Figure 8** when T approaches T_{Crit} , which explains that near the phase transition, it becomes more and more difficult to provide a sufficiently large number of electron pairs to support J_{Crit} , for zero loss current transport of practical value.

The result obtained in **Figure 8** is at least qualitatively in agreement with an analytical solution reported in the study of Flik and Tien [15], by the sharp decrease of $n_s(T)$ when T very close approaches T_{Crit} . A critique of this solution presented in the study [12] explains the differences seen in **Figure 8** between the two approaches.

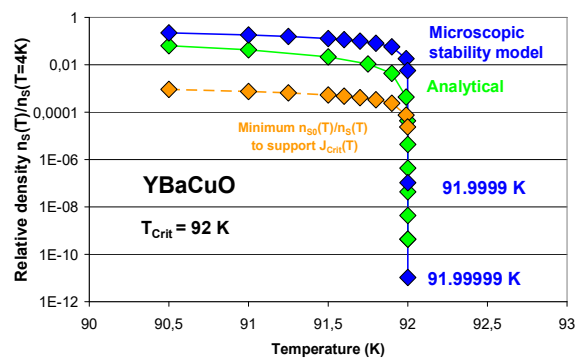


Figure 8. Relative density f_s , the order parameter defined as $f_s = n_s(T)/n_s(T = 4K)$ of electron pairs (dark-blue diamonds), in dependence of temperature, calculated for the YBaCuO 123 superconductor during warm-up. Reprinted from J. Supercond. Novel Magnetism 32 (2019) 1529–1569, Figure 11b.

From density f_s , relaxation rates are obtained as df_s/dt . Dark-yellow diamonds indicate minimum relative density of electron pairs that would be necessary to support a critical current of density 3×10^{10} A/m² in this superconductor, at 77 K and in zero magnetic field. The diagram compares predictions of the microscopic stability model [11]

with analytical results (light green, from the study of Flik and Tien [15]). Decay rates calculated from this figure are shown in **Figure 9**. Compare figure caption to **Figure 7**.

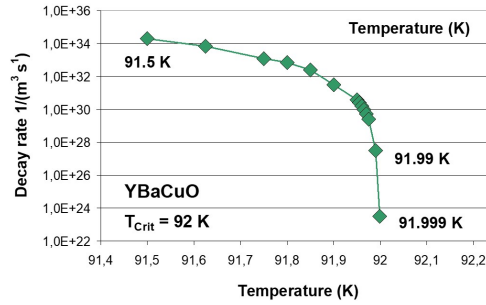


Figure 9. Repair rates, $dn(t)/dt$, of excited electrons (lifetime of the disturbed state) and decay rates, $dn_S(t)/dt$, of electron pairs (that in this numerical model equals the repair rates of electrons) in YBaCuO 123 at temperature very close to critical temperature, $T_{Crit} = 92$ K.

At $T = 91.99$ K and even more at $T = 91.999$ K, the system, though in dynamical equilibrium, should increasingly be unstable in relation to the state at $T = 91.5$ K or to any other, earlier state because of the fast decrease of the decay rates with increasing temperature. This must be reflected by the entropy differences calculated in Sect. 4. Compare figure caption to **Figure 7** that applies to also this figure.

This corollary of the model [11] accordingly predicts that quench might be initialized, and possibly become inevitable as soon as local temperatures, $T(x, y, t)$, well below critical temperature, $T_{Crit}(x, y, t)$, exceeds a second critical value, T_{Quench} (the points of intersections, here the temperatures $T_{1,2}$). Quench would become inevitable not just at T_{Crit} , the standard assumption, but earlier in the $n_S(x, y, t)$ vs. T -diagram. Incomplete relaxation then would not provide J_{Crit} large enough to allow substantial zero-loss current transport, at least in energy technology.

This is in strong contrast to all traditional stability models and to all existing stability calculations that agree a quench of the superconductor occurs only if sample temperature exceeds standard critical temperature, $T_{Crit}(x, y, t)$.

The principal existence of T_{Quench} , while already obvious from **Figure 7**, has to be discussed either in case of J_{Crit} -measurements (Sect. 3.1) which typically are realized in longer, practical time intervals (much longer than the intervals δt assumed in **Figure 7**) and at constant temperatures, or in case experiments are performed under continuously increasing temperature, like in a resistive current limiter. This case will be discussed in Sect. 3.2.

3.1. Constant sample temperature, like in J_{Crit} -measurements

Standard experiments to measure critical current density usually are performed in discrete time steps of extended length (against the δt applied in **Figure 7**), practically in the order of seconds, preferentially within minutes. This yields a series of $J_{Crit}[T(t)]$ taken at selected discrete temperatures, $T(t)$, with the T mostly given by decision of the experimenters or from time constraints arising from the experimental set-up.

If, and only if, the relaxation process can be completed, within the δt , at time intervals between successive measurements of J_{Crit} , which means if relaxation time $\tau < \delta t$, no repair steps are left to be performed, and the $J_{Crit}[T(x, y, t_{Eq})]$, are the dynamic equilibrium values. These, and only these should be accepted for calculation of any J_{Crit} -

dependent variables within periods δt , like for dimensioning superconductor cables for magnets, transformers or current limiters.

However, if $\tau > \delta t$, which may happen when after a disturbance, the electron system is already close to the thermal phase transition from super- to normal conduction at T_{Crit} (**Figure 7**), a large number, N_{nonEq} , of single electrons (residual decay products) would remain that have not been, and cannot be, re-organised to electron pairs and therefore do not result in a new thermodynamic equilibrium. This means: It is only a reduced number of electron pairs (reduced against the dynamic equilibrium value, at the given temperature) that partly, by a possibly strongly reduced J_{Crit} level, would be able to contribute to zero-loss current transport. This is not an equilibrium situation.

Fortunately, residual decay products left at discrete temperatures in standard J_{Crit} -measurements, or single electrons (provided from the shaded light-green and dark-blue sections in **Figure 1**) yet have the potential to be re-organised to electron pairs, if the lengths, δt , between successive measurements, efficiently could be extended. If they can be extended, they give the electron system more time to complete its total relaxation. This can be realised, for example, and trivially, by increase of cooling rates or by reducing transport current or magnetic field.

3.2. Continuously increasing temperature, like in a resistive current limiter

The temperature T_{Quench} is the limit below which all decay products, given in relative units, $f_S = n_S(T)/n_S(T=4\text{ K})$, can potentially be reorganised to electron pairs within a given period. At $T < T_{Quench}$, the number f_S equals 1, while at $T = T_{Crit}$, we have $f_S = 0$ (compare **Figure 10**).

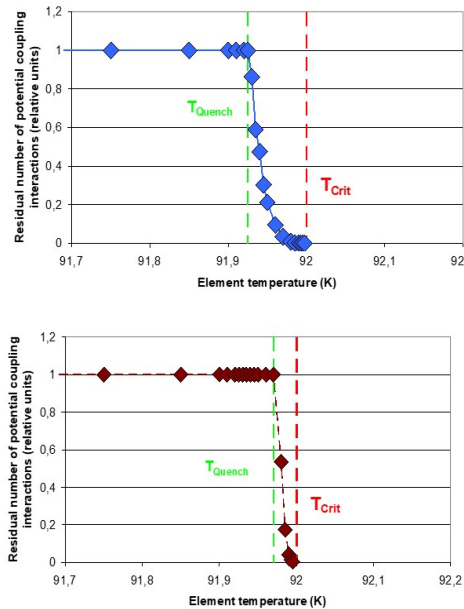


Figure 10. Residual number, N_{Eq} , of electron pairs (relative numbers). Reprinted from J. Supercond. Novel Magnetism 31 (2018) 959–979, first published in: arXiv 2212.09333 (Dec 2022), Figure 13a.

As a consequence, within $T < T_{Quench}$, relaxation safely will be, but between $T_{Quench} \leq T \leq T_{Crit}$ potentially could be completed, in the latter case not without additional actions taken by the experimenters.

The corresponding number, $1 - N_{Eq}$, of non-condensed single electrons, as decay products from a previous thermodynamic equilibrium state, increases with temperature. Temperature T_{Quench} is obtained in **Figure 7** from the intersection (open circles) of the curve relaxation time, τ , vs. temperature, T , with the horizontal δt -levels. Decreasing the process time intervals, δt , from 50 μs (above) to 1 μs (below) is used to approach a continuous warm-up process (like in operation of a current limiter) where continuously $\delta t \rightarrow 0$. As a result, dynamic equilibrium cannot be obtained (the system is not given enough time to relax completely). As soon as element temperature exceeds the limit $T_{Quench} = 91.925$ or 91.995 K, respectively, at least one but potentially *all* coupling “channels” become closed. The electron system then remains in a local, highly disturbed, non-equilibrium but still dynamical state. Part of the results was shown already in Fig. 11 [12].

Conversely, the number $(1 - f_s)$, again in relative units, denotes the number of electron pairs that within the given simulation or operation time, δt , cannot be obtained by condensation or re-condensation of all available single electrons.

At $T < T_{Quench}$, the number N_{NonEq} of residual, *uncoupled* electrons, if they result from previous decay of pairs, accordingly is zero, while at $T > T_{Quench}$ the number N increases very strongly, $N_{NonEq} = 2(1 - f_s) n_s(T_0)$, until at T_{Crit} all electrons remain uncoupled. Trivially, the resistance then would become Ohmic, with all current transport “channels” switched in parallel. The number N_{nonEq} could be measured by electron spin resonance.

The N_{nonEq} , as they cannot contribute to equilibrium, to zero loss current transport, to full levitation (“full” means: to stable levitation position) and, therefore, also cannot contribute to stability of the superconductor, increase the resistance of the whole electron body. But if the number N_{Eq} , the number of electron pairs, is not zero (strictly speaking: if it is still large enough to in parallel by-pass Ohmic resistances, zero loss current transport, at reduced J_{Crit} , would be possible). A check of whether, and to which extent this can clearly be realized and might be interesting for technical applications of superconductivity, can be performed by calculation of stability functions, $\Phi(t)$:

For $\Phi(t)$, we have to integrate, at given time t , the J_{Crit} over all positions (x, y) of conductor cross section,

$$0 \leq \Phi(t) = 1 - \int J_{Crit}[T(x,y,t), B(x,y,t)] dA / \int J_{Crit}[T(x,y,t_0), B(x,y,t_0)] dA \leq 1 \quad (1)$$

using differential cross section elements, this can be approximated by

$$0 \leq \Phi(t) = 1 - \sum J_{Crit}[T(x,y,t), B(x,y,t)] dA / \sum J_{Crit}[T(x,y,t_0), B(x,y,t_0)] dA \leq 1 \quad (2)$$

The summations have to be taken over all superconductor elements of the sample, with their individual J_{Crit} and small, but finite cross sections, dA . Equations (1) and (2) have been applied in previous papers of the author [6–9]. Later, results of sample calculations of $\Phi(t)$ show $\Phi(t)$ under solid conduction plus radiation heat transfer within the superconductor (and solid/liquid heat transfer at the solid/coolant contacts) in the thin film, YBaCuO 123 material. Results apply to turns 96 to 100 of coated conductor windings (see later, **Figure 15**). The calculations assume sudden increase of transport current above its nominal value beginning at $t = 3$ ms after start of the simulations. Flux flow resistances then are responsible for thermal losses that locally increase conductor temperature.

The stability function assumes values $0 \leq \Phi(t) \leq 1$ of which $\Phi(t) = 0$ is the optimum (for zero-loss current transport) and $\Phi(t) = 1$ the worst case where zero loss current transport is no longer possible.

Note the strong dependency of $\Phi(t)$ under variations of the exponent n in the relation $J_{Crit}(t) = J_{Crit,0} (1 - T/T_{Crit})^n$. Successful application of Equations (1) and (2) therefore requires precise, as far as possible, determination of the functional dependency of $J_{Crit}(t)$ on temperature.

A warning sign shall be issued: The condition $\Phi(t) < 1$ does not guarantee that no hot spot will be generated in the conductor cross section and during the whole time interval within which $\Phi(t)$ is calculated.

Maximum, zero loss current transport is given by

$$I_{max}(t) = J_{Crit} [T(x, y, t_0)] [1 - \Phi(t)] A_{SC} \quad (3)$$

with A_{SC} the total superconductor cross section. Time $t_0 = 0$ denotes start of the present simulation; at this time, all element temperatures are at their original values. Equation (3) follows immediately from Equations (1) and (2).

According to Equations (1) and (2), $\Phi(t_0) = 0$ at $t_0 = 0$, and both critical current densities, $J_{Crit}(x, y, t_0)$, and zero-loss transport current are maximum. The distribution of J_{Crit} accordingly would be uniform at t_0 , apart from statistical fluctuations of J_{Crit0} that might be caused by possibly existing deficiencies in materials preparation and handling. But homogeneity is quickly lost at times $t > t_0$.

The results obtained for the residual number N_{nonEq} can also be re-plotted (**Figure 11**) in terms of relaxation time t_{Eq} (instead of temperature, **Figure 10**) at which the system arrives at T_{Eq} (this again is shown only for the case $T_{Quench} = 91.925$ K, $\delta t = 1$ μ s, lower diagram of **Figure 10**).

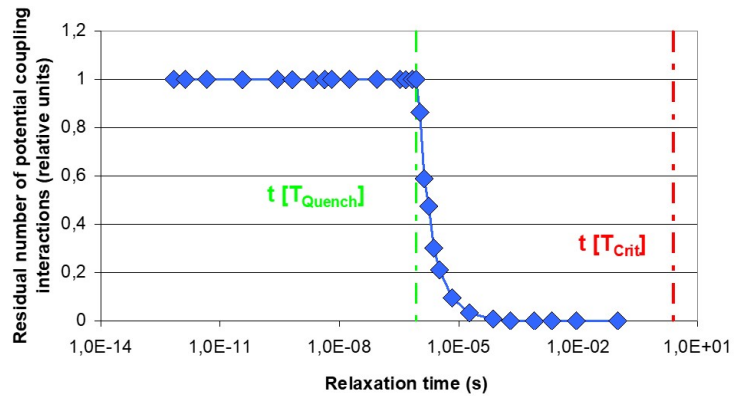


Figure 11. Same results as in **Figure 10** (upper diagram), but here vs. relaxation time, τ , using $T_{Quench} = 91.925$ K that corresponds to $\tau = 8.388 \times 10^{-7}$ s (only this case is plotted).

The difference between times t_{Quench} and t_{Crit} , at which the curve reaches temperatures T_{Quench} and T_{Crit} (light-green and red, dashed vertical lines) defines length of an at least partly dead time interval within which zero-loss current transport might no longer be possible at all or at only reduced critical current density. The figure accordingly shows the residual number of electron pairs (relative numbers) that within $T < T_{Quench}$ safely will be, but between $T_{Quench} \leq T \leq T_{Crit}$ still could be completed, in the latter case only by additional actions taken by the experimenters. Within the interval between T_{Quench} and T_{Crit} , zero-loss current transport might no longer be possible at all or at only reduced critical current density. The red dashed line corresponds to a hypothetical $T = 91.995$ K when it approaches T_{Crit} . At still higher T , but below T_{Crit} , position of this line diverges, according to divergence of the relaxation time (**Figure 7**), on the horizontal simulation time scale.

Accordingly, the described approach to a new superconductor stability criterion, by considering T_{Quench} in addition to the standard T_{Crit} , defines temperature and time limits, namely to obtain (recover to) thermodynamic equilibrium,

- a temperature limit, $T_{Quench} < T_{Crit}$,
- a time limit, $t_{Eq}[T_{Quench}] \ll t_{Eq}[T_{Crit}]$

With increasing temperature, the limits approach T_{Crit} and $t_{Eq}(T_{Crit})$, respectively. If the limits are exceeded, both limits initiate quench of the superconductor that invariably will be realized completely if not additional measures are taken to increase effectively the length of the time intervals.

In summary of these predictions, the electron system not necessarily “has to wait” until its temperature finally, during a disturbance, exceeds T_{Crit} to generate Ohmic resistances. Limitations to critical current density, because of too small a number of available electron pairs, start earlier, already at T_{Quench} , not later and not only at T_{Crit} .

Temperature T_{Quench} therefore can be interpreted as a “point of no return” beyond which quench no longer can safely be avoided. The condition “ $T > T_{Quench}$?” can be identified as another stability criterion.

But the question is how T_{Quench} can be determined. Not just a trivial task, but see Sect. 7 of this paper for suggested experimental setup. The key is: Precise measurement of the electric field over the superconductor sample, under variation of current, as far as highest accuracy of the experiment can be realized with presently available experimental equipment. Or, as will be discussed in Sect. 7, measurement of levitation height or of levitation force in dependence of time.

Contrary to measurements of J_{Crit} at constant temperature, temperature in a current limiter under a fault current increase continuously. A problem then arises from understanding the process time intervals, δt , in **Figure 7**. Length of these intervals during continuous warm-up reduces to zero. Length δt then no longer is on the decision of the experimenters. Within intervals δt of zero length, relaxation because of the divergence of τ in **Figure 7**, so far could not be completed at any temperature below T_{Crit} . How can this problem be resolved?

Diffusion of heat, electric or magnetic field or current or of equilibrium charge distribution within infinitely small intervals dT and dt can be described by characteristic times, τ_{Th} , τ_m , τ_C , respectively, as is usually done in all diffusion models. For this purpose, it has to be shown that the τ_{Th} , τ_m , τ_C are very small to yield an approximate solution of the divergence problem arising from **Figure 7**.

The three characteristic diffusion times describe within which period of time, or over which distances, diffusion of the concerned variables cause substantial variations (reductions) of their magnitude, usually by exponential damping and with phase differences⁶.

Characteristic diffusion times thus indicate over which a “system” (here the superconductor material) imposes limits to propagation of the said variables into sample depth. The limits represent “quasi-operation intervals” of the system itself, existing without interventions by experimenters.

Length of these intervals (τ_{Th} , τ_m , τ_C) is estimated in the Appendix to this paper; each of these is between 10^{-7} and 10^{-6} s. Determination of relaxation time thus follows from the lower dashed horizontal line in **Figure 7**, and if temperature exceeds the intersection point, $T(\tau)$, relaxation no longer will be completed.

4. Entropy production during electron pair decay and relaxation

Decay rates of electron pairs from the excited YBaCuO 123, thin film superconductor is shown in **Figure 9**. After this decay, why should the decay products at all be motivated to re-combine (relax) to electron pairs and to thermodynamic equilibrium?

This question at first sight might appear trivial. But can it also be demonstrated, numerically or otherwise, and from the results be concluded that the relaxation process reduces entropy of the final (again equilibrium) state? And can correlation also between relaxation time and entropy, and between charge carrier density, $n_s(T)$, be demonstrated? Their correlation, if their existence could be demonstrated, would put the present procedure (estimating relaxation time) on safe grounds.

Calculation of the entropy in the following is performed as in case of mixing entropy of two ideal gases. Initially, the gases each are assumed to occupy constant volumes V_1 and V_2 contained in a closed, constant total volume, $V = V_1 + V_2$. As soon as an un-permeable wall that separates V_1 from V_2 is removed, the two gases diffuse into each other. Calculation of the entropy assumes that both gases behave as if the other is not present at all. This situation resembles penetration of two sets of electrons into each other. Since the rate of electron/electron scattering is very small, regardless of their spin orientations, the sets behave as if the other is not present.

The mixing of two ideal gases and entropy production is explained by Falk and Ruppel [16] (“Energy and Entropy” by G. Falk and R. Ruppel). The solution can be found in its Chaps. 16, 19 and 20 (indicating single equations would not be very helpful because of the complexity of the entropy problem).

For decay of electron pairs and their relaxation, instead of expanding two ideal gases, we formally consider two sorts of electrons, i) decay products (normal conducting electrons or quasi-particles) and ii) the electrons that already have recombined to superconducting electron pairs.

But both sorts of electrons are identical: i) single electrons, as Fermions, that cannot be distinguished, and ii) electron pairs, composed of other identical electrons, a situation that can be seen as correlation of two single electrons that in dynamic equilibrium continuously decay and recombine, at any temperature above zero.

But if seen from the energy aspect, electrons in the ground state (electron pairs) and excited electron states (single electrons above the energy gap) are separated by at least the width of the gap. After completion of decay of pairs and during the relaxation processes, they expand to the final total state, with N_{Total} electrons that comprise the remaining single, normal N_1 conducting electrons and N_2 the electrons that are correlated to pairs. “Correlation” means with no change of their nature (unit quantum of electrical charge) or origin (Fermions, that remain Fermions even if separated on the energy scale by the energy gap) with $N_{Total} = N_1 + N_2$. All their constituents are identical.

The next question then is whether electrons originating from decay of electron pairs may be considered not only as identical but also as absolutely independent particles for the suggested entropy calculations.

Electrons, because of their electrical charge, may be seen as quasi-particles (a mathematical concept to incorporate a “queue” of interactions arising during motion through the ion lattice). But also quasi-particle can be treated as independent of the others⁷. We have taken this into account during the calculations in the study [11] by screening factors, χ , that essentially modify the dielectric constant. In the solid, the

electrostatic (repulsive) Coulomb potential consists of (a) the repulsive interaction (interpreted as a mean field), and (b) the (attractive) positive ion charges in the solid. The two contributions are superimposed. The Thomas-Fermi potential, as the classical example of a screened Coulomb potential, was well approximated by application of the χ to the proper Coulomb potential. It is within this approximation (by integration of their interactions with other quasi-particles and with the lattice, all treated as identical) that electrons can be considered also as independent of each other in the entropy calculations performed in the following.

The entropy difference of two ideal gases that initially occupy volumes, V_i , and that expand to the total volume, V_f , by analogy transfers from to the entropy difference of two ideal gases to the two indistinguishable sorts of electrons.

$$\Delta e_i - \Delta e_f = N k \ln (V_f/V_i) \quad (4)$$

$$\Delta e_i - \Delta e_f = 1/T_{i,f} \ln [N_f(T_{i,f})/N_i(T_{i,f})] \quad (5)$$

Particle number, N , replaces volume, V , because both N and V are extensive variables, in the sense of the Gibb's fundamental, total differential dE (expansion of dE in a series of products $Z_i dX_i$ wherein both Z and X are physical observables). This yields, for example, $dE = TdS - pdV + \mu dN$ for a single component gas. Z denotes the *intensive* variable (in this example, T , p , μ , and X the extensive variable (S , V , N); μ denotes the chemical potential.

The electrons, N_i , at given temperatures T_i (during the decay and relaxation processes) “expand” (fill-up) to their final number, N_f , like volumes V_i expand to final V_f .

Absolute values of entropy cannot be calculated. Only entropy differences can be found, between temperatures, T_i and T_f , in Equation (5), and particle numbers, $N_{i,f}$. Temperatures T_i and T_f in Equation (5) are not identical: Decay of electron pairs is initialized just by temperature increase from T_i to T_f (otherwise there would be no decay), but relaxation occurs, and is completed, at the final T_f that results from the disturbance (the system does not cool-down under relaxation; we are in a warm-up process, the associated temperature *increase* generates the disturbance). Relaxation of the electron system is not subject to thermal energy transfer or temperature exchange but is solely a quantum-mechanically driven, entropy-decreasing selection process.

Results of the calculation of the decay rates, ΔS_1 , and of the total process (decay followed by relaxation), $\Delta S_1 + \Delta S_2$, are shown in **Figure 12**). The value $T_i = 91$ K is arbitrarily chosen; other values $77 \leq T < T_{Crit}$, too, would allow calculation of entropy change (except for limitations by computational efforts).

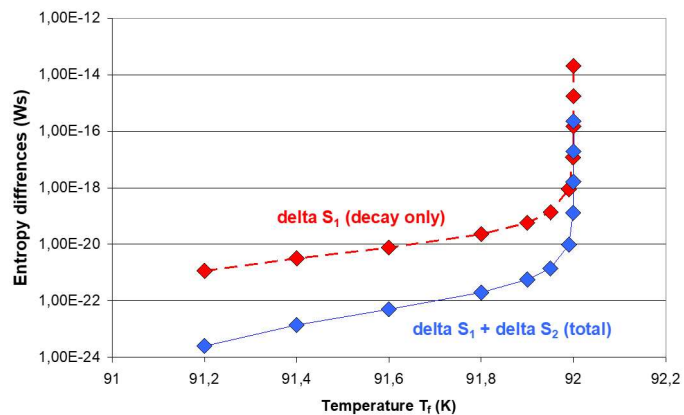


Figure 12. Entropy differences, ΔS , calculated using Equations (4) and (5).

The results shown in **Figure 12** are obtained at initial (i) and finally (f) completed processes: (1) decay of electron pairs when temperature increases from initial T_i to final T_f (using $T_i = 91$ and $91.2 \leq T_f < 92$ K), followed by (2) re-condensation at the constant T_f , All S_I and $S_I + S_2$ are positive (while delta S_2 for the completed relaxation process (2) is negative), which in **Figure 12** reduces delta $S_I +$ delta S_2 (decay plus relaxation) to below delta S_I (decay only). This means increase of disorder and of entropy. The calculations take into account a possibly existing limit, the “availability” of the electrons for relaxation. The calculations apply any (relative) values, f_{rel} , between 0 and 1 of the total body of excited electrons. For the present figure, we have in a test calculation applied almost complete availability, f_{rel} very close to 1. The parameter “availability” in the present and in our previous papers (like Appendix A1 in the study of Reiss [13]) is used as just a statistical parameter. It checks sensitivity of the simulation results on the number of single electrons that must find partners for relaxation to pairs from the existing total body of temporarily uncoupled, “available” electrons

Why in **Figure 12** is delta $S_I +$ delta S_2 not zero? The results confirm the expectation that decay of electron pairs at any temperature below T_{Crit} , provides positive, while relaxation to pairs provides negative contributions to entropy production. Decay means transition from high order (pairs) to low order (unpaired electrons), and relaxation is the reverse process that reduces entropy of the electron system (here we have to note that we speak of entropy production, not of entropy exchange).

5. Correlations

In a superconductor, all currents flow with critical current density, J_{Crit} . If the standard relation, $J = n v e$, is provisionally transformed, from normal conductors to superconductors, we arrive at the same relation, but only under equilibrium conditions. If applied to superconductors, Equation (6) could be used at temperature clearly below T_{Crit} , in homogeneous material, again with uniform charge density distribution and without a magnetic field.

$$J_{Crit} = n_s v_{Fermi} 2e \tag{6}$$

But this is a very rough approximation only since the plot of J_{Crit} vs. n_s taken at same temperatures shows a quite different behaviour (**Figure 13**): Dependence of $J_{Crit}(T)$ on $n_s(T)$ in the thin film YBaCuO 123 superconductor appears to be strongly exponential.

While **Figure 13** apparently confirms an *expected* (one might even say: “felt”) physical, causal correlation between both variables, final proof by *numerical*, standard statistical methods still has to be given, see below.

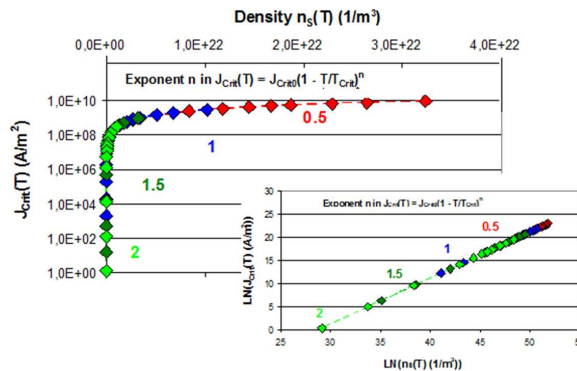


Figure 13. Relation between critical current density, $J_{Crit}(T)$, and density, $n_s(T)$, of electron pairs in YBaCuO 123 superconductor material.

Results are shown (upper diagram) for different values of the exponent n in the standard relation $J_{Crit} = J_{Crit0} (1 - T/T_{Crit})^n$. For $T = 77$ K, $J_{Crit} = 3 \times 10^{10}$ A/m², for all values of the anisotropy parameter $X = D_{ab}/D_c$. The figure solely applies equilibrium values of $J_{Crit}(T)$ and $n_S(T)$, compare text. The inset (lower diagram) shows the identical data but on double logarithmic scale. From solely physical aspects, the relation as a conclusion should be causal, not spurious. But tentative calculation of the correlation coefficient yields $r = 0.805$ that indicates only weak (if any) correlation.

We therefore make a second correlation attempt, again provisionally in a simple plotlike **Figure 13**, here between entropy differences, S_2 , of the relaxation process after its completion, with relaxation time, τ , all in dependence of temperature ($91 \leq T_f < 92$ K). The result is shown in **Figure 14**:

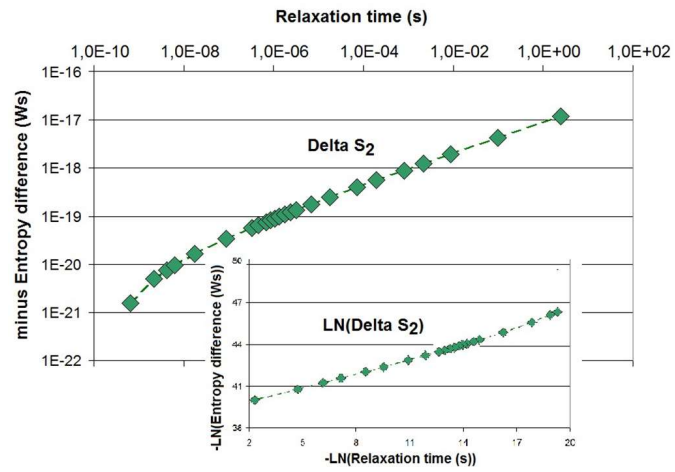


Figure 14. Correlation of entropy difference, S_2 , with relaxation time, τ , after completion of the relaxation process.

Note the double logarithmic scale in the upper diagram. The inset (below) shows that on double logarithmic scale the relation between entropy difference, S_2 , and relaxation time, τ , is approximately linear, which reflects the value of the correlation coefficient, $r = 0.933$. The values of relaxation time (and the temperatures at which these are obtained from the model [11]) are those of **Figure 7**.

The more the system approaches T_{Crit} , or the larger the relaxation time, the more negative becomes the difference, ΔS_2 , between the entropy at $T_i = 91$ K (with T_i the said, arbitrary reference value) and at $91 \leq T_f < 92$ K (with T_f the temperature to which temperature increases under a disturbance). The difference ΔS_2 does not become positive anywhere on the horizontal scale, τ , in **Figure 14** (note the double logarithmic scale and the plot of minus ΔS_2).

The driving force onto the system to relax to an equilibrium state (the entropy change) increases the more the temperature approaches critical temperature!

But there are problems: Correlations can be causal or spurious, and it is not clear that they always would be transitive. This means, if there are correlations between variables V_1 and V_2 , and between V_2 and another variable, V_3 , it is not clear that V_1 uniquely would be correlated also with V_3 . In the present case, this means it is *not* clear that the two following, obviously physical causal correlations between V_1 and V_2 , i.e. between T and $J_{Crit}(T)$, and between V_1 and V_3 , i.e. between T and electron pair density, $n_S(T)$, above the energy gap, with an appropriate temperature dependence⁹ would be transitive so that also V_2 and V_3 , i.e. $J_{Crit}(T)$ uniquely would be correlated with $n_S(T)$.

It is not sufficient to rely on the common dependency on temperature of both variables V_2 and V_3 . Instead, the correlation between V_2 and V_3 is *uniquely* fulfilled only if also the temperature dependency of both V_2 and V_3 is uniquely defined, i.e. if both V_2 and V_3 in parallel and in equal-directional increase or decrease with temperature.

Fortunately, both variables, $J_{Crit}(T)$ and $n_S(T)$, decrease with increasing temperature, as is well known. From the physics aspect, this speaks in favour of causal correlation¹⁰.

The $n_S(T)$ used on the abscissa of **Figure 13** are equilibrium values only if $T < T_{Quench}$. If during measurements of J_{Crit} the system is given more time (seconds to minutes) to complete relaxation, the range of validity of the abscissa values in this figure within which correlation could be confirmed, would increase to values beyond this T_{Quench} and beyond also to τ_1 .

Support of the correlation between J_{Crit} and $n_S(T)/n_S(T_0)$ and strength of the correlation between relaxation time, τ , and entropy differences, S_2 , now shall be found by application of elementary statistical methods described in standard textbooks on statistics (e.g. [17]).

First, consider a number of N value pairs $(x_1, y_1), (x_2, y_2), \dots (x_N, y_N)$ which within $77 \leq T \leq T_{Quench}$ are applied as two sets (i and ii), a number of N value pairs $(J_{Crit(1)}, n_{S(1)}), (J_{Crit(2)}, n_{S(2)}), \dots (J_{Crit(N)}, n_{S(N)})$ comprising critical current and electron pair densities, $J_{Crit}(T)$ and $n_S(T)$, both at temperature, T (set 1) a number of N value pairs $(S_{2(1)}, \tau_{(1)}), (S_{2(1)}, \tau_{(1)}), \dots (S_{2(N)}, \tau_{(N)})$ comprising entropy differences, $S_2 = \Delta e_i - \Delta e_f$, see, Equation (5), and relaxation times, τ (set 2).

J_{Crit} and n_S depend on temperature and are separately calculated, which means J_{Crit} and T , and n_S and T , are strongly correlated, but the correlation analysis should demonstrate that also J_{Crit} and n_S are correlated.

For this test, we use a finite number N of value pairs that represent sections of the corresponding, in principle unlimited, parent populations.

The calculations apply the data shown in **Figures 12–14** (pairwise considered, at same temperature).

First, the anticipated correlation between $J_{Crit}(T)$ and $n_S(T)$, solely from physics behind, seems to be reasonable (large current needs large number of charge carriers), but correlation is strongly questionable, from *formal* aspects of correlation analysis, in view of the strongly non-linear increase of $J_{Crit}(T)$ with increasing $n_S(T)$, see the upper diagram in **Figure 13**.

Only when re-plotting this diagram on logarithmic scales, the observed linear increase (lower diagram in **Figure 13**) suggests that the correlation coefficient, r , should not be too small (not very small against $r = 1$). But the tentatively calculated result using standard relations for variances and co-variances yields finally $r = 0.805$ for set 1 of $N = 21$ data pairs. Correlation thus is weak, at the best.

An explanation is: While the relation between $J_{Crit}(T)$ and T is analytical and both variables, from physical reasons, must be correlated, the density, $n_S(T)$, as it results from the model [11], is only statistically correlated with T , so that a correlation between J_{Crit} and n_S , other than from physical background, remains doubtful.

The situation with S_2 and T , and τ and T seems to be different. Solely from physics behind (Sect. 4), the entropy difference, S_2 , should more definitely be correlated with relaxation time, τ , than J_{Crit} with the statistical n_S . **Figure 14** (upper and lower diagram) demonstrates that this expectation really seems to be fulfilled, we have $r = 0.933$, for set 2 of $N = 13$ data pairs, which is, in the meaning of correlations, much better than the value $r = 0.805$.

It is therefore expected for set 2 (entropy difference, S_2 , vs. relaxation time, τ) that both reflect the identical physical process (relaxation), both are correlated, and therefore, entropy is the driving force for relaxation.

6. Overall concept to simulate total thermal energy transfer through superconductors

6.1. Motivation from thin film, normal conductor investigation

The procedure originates from a numerical method [18–22] to remotely determine thermal diffusivity of transparent or semitransparent thin films. The papers suggest a “Front Face Flash Method”. The experiments require laser pulses of very short duration (like 8 ns in our papers) onto a “target” (like the red solid circle in **Figure 4**) and fast measurements of transient temperature excursions.

Instead of taking temperatures directly in the pulsed heating region or on the rear sample surface, the method works also when it takes temperature solely at the front side and, which has a great advantage, at any distance from the irradiated target [18–22] for more detailed descriptions. It is sufficient to take data in only radial directions, which by both simplifications demonstrates great flexibility of the method. Flexibility was also demonstrated, after only slight modifications, to apply principles of the method to an exotic situation¹¹.

In an extension of the simulations reported in studies [18–22] to superconductors in the present paper, the core of the method is to numerically calculate solutions of Fourier’s differential equation, see below, Equation (10), If extended to inclusion of radiative diffusion, Equation (13), the solution shall be found also in complicated geometry and boundary conditions and with all heat transfer mechanisms (transport “channels”) included that contribute to total thermal transport within the samples and at boundaries to different, neighboring materials.

The numerical procedure involves Finite Element and Monte Carlo simulations. It was applied first to non-conductors. Transient temperature distributions were obtained using experimentally known ZrO_2 and SiC thermal diffusivity, solid conduction and extinction coefficients (but in principle, the calculations could be performed to any thin solid).

For a test of the method, simulated temperature distributions obtained by the FE method that used the thermal diffusivity, D , as input into the calculations, was applied to in turn extract the diffusivity from the calculated results for $T(x, y, t)$ by application of Equation (8), see below (the diffusivity, D , accordingly was extracted from the output of the calculations and, hopefully would equally reproduce its input value).

Equation (7) is standard, but Equation (8) was derived before 1999 by the late co-author, Oleg Yu. Troitsky, of our papers, see the reference list. The origin of this expression is found in a superposition method that was presented in a paper on the pulse method by Grigoriev (for its citation see the study of Troitsky and Reiss [18]). As a great success, the method was confirmed, see below.

Transfer of the numerical method, from thin film normal conductors to superconductors, was made by considering the (1 G) multi-filamentary BSCCO superconductor with its geometry already shown in **Figure 3**, and the coil prepared with 100 turns from the (2 G), coated thin film YBaCuO 123 superconductor of which the

geometry (the cross section in one single turn was shown in **Figure 4**). Coil architecture and its details are shown in **Figure 15**.

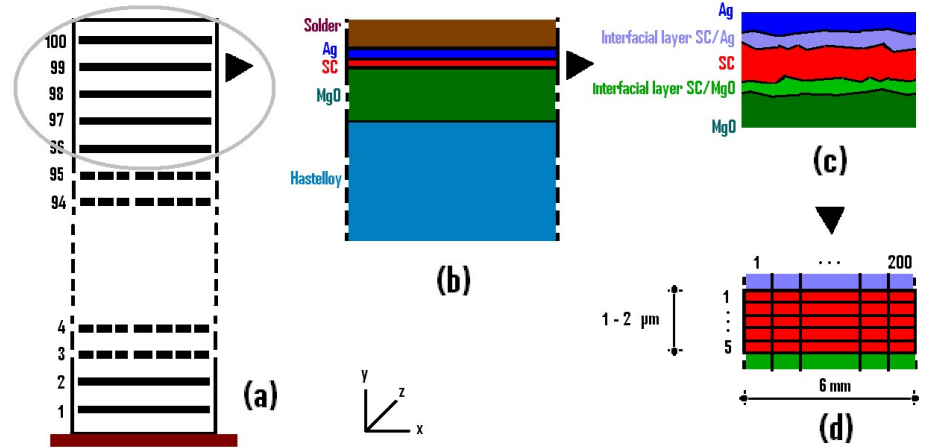


Figure 15. Principal Finite Element simulation scheme of a coil and its thin film conductor geometry (schematic, not to scale. Reprinted from J. Supercond. Novel Magnetism 31 (2018) 959, Figure 1.

Figure 15(a) shows the coil consisting of 100 turns of the “second generation” (2G) coated, YBaCuO 123 thin film superconductor (**Figure 4**) of which only turns 96 to 100 are simulated, **Figure 15(b)** layers in immediate neighbourhood of the superconductor (SC) thin film (as an example in turn 99), **Figure 15(c)** overview of turn 99 showing simulated, very thin interfacial layers between superconductor film and Ag (metallization) and between superconductor and MgO (buffer layer; dimension of the roughness is highly exaggerated in this diagram of which details used in the numerical calculations are shown in **Figure 15(d)**), with cross section and meshing of the superconductor thin film in one turn. Superconductor layer thickness is $2 \mu\text{m}$, its width is 6 mm, thickness and width of the Ag elements is like the data of the superconductor thin films. Crystallographic c-axis of the YBaCuO-layers is parallel to y-axis of the overall coordinate system. Thickness of the interfacial layers is estimated as 40 nm. In SC, Ag and interfacial layers, we have 5×200 -line divisions for creation of the Finite Element mesh.

The analysis was confined to isotropic (constant, independent of temperature) materials properties (conductivity, specific heat, extinction coefficient, albedo), i.e. to idealistic conditions. But the procedures in principle are straightforward (though becoming increasingly laborious) when analysis is performed for anisotropic, temperature or wavelength-dependent parameters, or for layered samples.

In a step 1, thermal homogeneity, $T_0(x, t)$, at any constant sample depth y , preferentially at $y = 0$, has to be controlled, for its origin see the study of Reiss and Troitsky [21,22],

$$T_0(t) = [T(t)/t]/[dT(t)/dt] \quad (7)$$

It identifies the region of Fourier numbers, $F_o = Dt/L^2$ (using $0.16 \leq F_o \leq 0.25$), to yield the time interval during which the heating regime is regular and where Step (2), below, may be applied to measured temperature excursions, $T(t)$. Results for $T_0(t)$ are shown in the study of Troitsky and Reiss [22], its Figs 10a–11b (it would be useless to apply the Front Face Flash method, step 2, to regions where $T_0(t)$ oscillates).

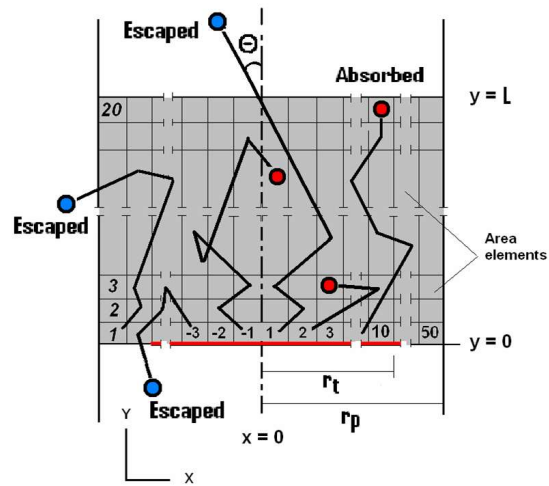


Figure 16. Horizontal section of a cylindrical pellet of radius, r_p , or a cylindrical section of a thin film (schematic). The figure is copied from Fig. 6b [8]. First published in arXiv 2212.09333 (Dec 2022), Figure 3.

The conductor section shown in **Figure 16** includes the symmetry axis ($x = 0$, thick dashed-dotted line). Right and left halves of the pellet are divided each into a number of 1000 area elements ($i \leq 50, j \leq 20$) that are meshed with in total about 8×10^4 plane finite (FE) elements (not shown in this figure). Area elements (i, j) are indicated dark-grey, and radiation bundles by thick black lines. Rotation of the area elements against the axis of symmetry ($x = 0$) generates volumes elements (cylindrical concentric shells). The target of radius $r_t = 120$ mm, identified by the horizontal thick red line, is irradiated or otherwise flash-heated during 8 ns (rectangular pulse), with uniform total energy depositions, Q_0 (Ws), onto the target elements (volume elements, cylindrical shells occupying the first row, $j = 1$, of the discrete co-ordinates i, j); since their cross sections increases with distance from $x = 0$, thermal power (W/m^2) decreases with larger co-ordinates, x . Scattering angle is denoted by θ . Bundles either are absorbed/remitted (red circles) or scattered and may escape from the sample (blue circles, index “Escaped”) after a series of absorption/remission or scattering interactions within the sample material. The scheme is used in both Monte Carlo and Finite Element (FE) calculations. The figure is copied from Fig. 3a [9].

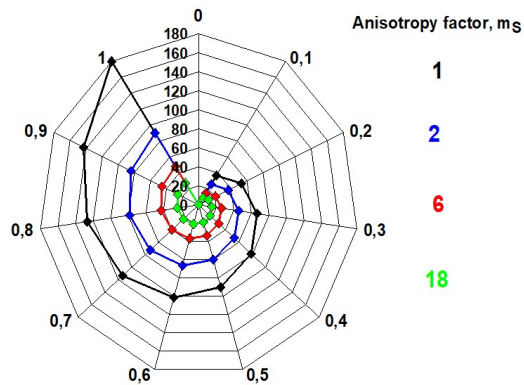


Figure 17. Angular distribution (spider diagram) of bundles remitted from volume elements, in dependence of anisotropy factor, m_s (solid symbols) and random variable, $0 \leq R(\theta) \leq 1$ (on the periphery, in steps of 0.1). Reprinted from Horizons in World Physics 276 (2012) Chap. 1, Sect. 9, Figure A1.

The diagram illustrates that remission or scattering angles, $0 \leq \theta \leq 180^\circ$ (ordinate), are the smaller the larger m_s . For example, if $m_s = 18$ and $R(\theta) = 1$, the cone angle $\theta < 27.3^\circ$ against normal to the surface is identified from the ordinate. The figure is copied from the study of Reiss and Troitsky [21].

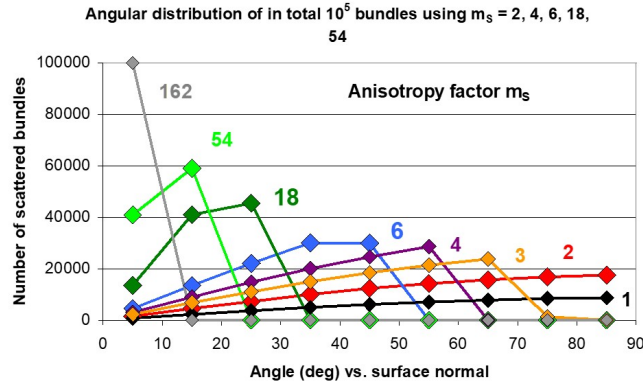


Figure 18. Scattering phase function, Ψ , calculated from a total set of bundles ($M = 10^5$) in the Monte Carlo simulation and with random values $R(\theta)$. Reprinted from J. Supercond. Novel Magnetism 33 (2020) 3279–3311, Figure 8a.

The phase function is represented by the number of bundles, $n(\theta)$, scattered under angles, θ , within the conductor against surface normal of concentric rings (generated by rotation of the plane elements, **Figure 16**). Results apply to the $2 \mu\text{m}$ thin film YBaCuO 123 superconductor and are given for different values of the (scattering) anisotropy factor, m_s , at mid positions within $\Delta\theta = 10 \text{ deg}$ intervals. The larger the values of m_s , the more bundles are concentrated at small (forward) scattering angles. When $m_s = 162$ (light-grey diamonds), the bundles are sharply focussed to $\theta < 10 \text{ deg}$.

For Step (2), the diffusivity, D , was extracted from absolute temperatures, T_i^k , by the following approximation [22].

$$D = \frac{\frac{T_i^k - T_i^{k-1}}{\Delta t}}{\frac{T_{i+1}^k - T_{i-1}^k}{2r_i \Delta r} + \frac{T_{i+1}^k - 2T_i^k + T_{i-1}^k}{(\Delta r)^2}} \quad (8)$$

It replaces the analytical solution for radial heat flow, usually an infinite series expansion, by a comparatively simple, straight-forward finite difference relation. The T_i^k , with indices i and k , denote temperature measured or simulated at time, t^k , at position number, i , with $r = r_i$ at front sample surface ($y = 0$); the co-ordinate r is parallel to x -direction. Time and radial co-ordinate intervals are defined by $\Delta t = t_k - t_{k-1} = t_{k+1} - t_k$, and $\Delta r = r_{i+1} - r_i$. The r_{i+1} and r_i are taken outside the target. Temperatures applied in Equation (8) are nodal values. With the fine mesh and correspondingly improved spatial resolution, divisions by zero in Equation (8) are avoided.

For solely solid conduction, there is good (SiC) and in case of ZrO_2 almost perfect agreement, for thin film Cu and AlN samples where the extracted diffusivity reproduces the reference values of D within just 4 to 8 per cent uncertainty (note that measurement of thermal conductivity and of diffusivity is extremely difficult to be realized if the uncertainty shall be below 10 per cent). Also, literature values of the diffusivity, D , of SiC and ZrO_2 ceramics are strongly different, by more than one order of magnitude, and the D of AlN is very large (it exceeds the D even of metallic Al).

Accordingly, we were motivated to apply the numerical method to also superconductors, to thin film samples. Extension of the Front Face Flash method to superconductors introduces a solely diffusion heat transfer-oriented method to investigation of radiation contribution to total heat flux in these materials. This is a new method to complete investigations of superconductor stability.

Temperature distributions obtained in simulations, or in experiments with superconductors, constitute the basis from which all conclusions and predictions in the present paper have been drawn.

6.2. Overview: How to numerically simulate temperature fields and to avoid quench

From a general viewpoint, the stability investigations in this paper are predominantly oriented on simulation and analysis of transient temperature fields. These are subsequently applied to determine electrical and magnetic properties using empirical relations. These are relevant for description of the energy balances in the superconductors. Both temperature and magnetic field are thermodynamic variables, while critical current is not. This suggests treatment of the stability problem from predominantly energy balances. All results are local values, with space and time resolutions as far as available from converged numerical simulation in complicated conductor architecture.

The method does *not* treat the stability problem as a continuum problem. This is contrary to the continuum approximations and H-formulations, the solution of Maxwell's equations, reported by different authors in contributions to the International Workshops on Numerical Modelling of High Temperature Superconductors (the "HTS mod" workshops). Continuum approximations of in reality highly detailed superconductor geometry and materials compositions neglect variations of just the very detailed superconductor tape and cable architectures, in particular the electrical, interfacial resistances between different grains or layers in filamentary and thin film superconductors, respectively. Readers are kindly invited to think over relevance of this approximation and report possibly existing justifications to the author.

Interfacial resistances not only constitute barriers against thermal energy flow but also allocate the very critical, weak-link problem arising in superconductor materials development and applications. A continuum theory hardly can be expected to yield reliable solutions in tiny filaments and highly structured compositions of thin film arrays, all of very small thickness, of strongly different materials properties and of strongly anisotropic transport properties, see later.

It is also important to note that analytical or numerical methods, like Finite Element software, to solve Fourier's differential equation, yield stationary or transient temperature of the *lattice* of a superconductor, not of its electron system (except that after completion of relaxation both temperatures in the final equilibrium, numerical convergence state hopefully will coincide).

This is contrary to a description of how to obtain electron temperature in experiments [23] when normal conductors (metals) were exposed to powerful femto-second or pico-second laser pulses. Evolution with time of ion and electron temperatures were described separately using a transport equation, Equation (1) of this reference that considered divergences of thermal gradients multiplied by conductivities. But this does not apply to electron pairs since they do not experience thermal resistances (like there are

no electrical resistances except interfacial) that could support application of this method to also superconductors. As a consequence, the method suggested by Agranat et al. [23] also cannot deliver relaxation time.

Assume for the moment that the electromagnetic energy, E , provided by a transport current of momentary density, J , in a magnetic field, is distributed by a disturbance to the volume of a superconductor, a thin film, for example, wherein the source, E , leads to an increase of its temperature. A simple electrical/thermal energy balance (see below, Equation (9)) estimates the mean (stagnation) temperature, T_m , by conservation of energy, to which the system temperature gradually converges, assuming for simplicity adiabatic conditions. In Equation (9), ρ_{el} and ρ denote electrical resistivity and materials density, and c_p its specific heat. The electromagnetic energy shall be distributed, after each variation of J or of ρ_{el} , to the thin film. If then T_m exceeds T_{Crit} , the superconductor experiences the phase transition from superconducting to normal conducting state, the quench. Equation (9) thus constitutes an overall criterion how to determine stability. This means uncertainties in the prediction of quench by Equation (9) mainly relies on accuracy of simulated or measured temperature fields (by the way, the problem “accuracy” arises also when the second critical temperature, T_{Quench} , shall be determined (as mentioned already in part A, Sect. 3.2; Sect. 7 of this paper suggests high precision experiments that could yield the solution how to find this second critical temperature).

$$\int_0^{\infty} \rho_{el}(t) J^2(t) dt = \int_0^{T_m} \rho c_p(T) dT \quad (9)$$

Fourier’s differential equation, if considering, again for simplicity, only solid conduction is a special form of the continuity equation, $\partial \rho_Q / \partial t = \text{div } j_Q$, wherein j_Q denotes heat flow density and ρ_Q the density of thermal energy. If we accept that heat the quantity Q , an energy form, cannot be destroyed, Fourier’ differential equation reads [24],

$$\rho c_p dT/dt = \text{div } q + Q(t) \text{ (W/m}^3\text{)} \quad (10)$$

using the thermal conduction equation, in any conductor, here with $\lambda = \lambda_{Cond}$ the solid thermal conductivity, ρ the density of a substance (here the solid superconductor) and c_p its specific heat. From Equation (10), we have $D = \lambda / (\rho c_p)$, the thermal diffusivity.

$$q = - \lambda \text{ grad } T \text{ (W/m}^2\text{)} \quad (11)$$

The operators div and grad denote divergence (of the vector q , the conduction heat flow density) and gradient (of the temperature field), respectively. A term $Q(t) = Q(x, y, t)$ describing losses, e.g. to the coolant, at interfacial slid/liquid positions (x, y) ; it would be added appropriately to the thermal source function.

The solutions to obtain temperature excursions from Equations (10) and (13), below, in the present paper are calculated by the Finite Element method, in the simple cylindrical geometry in case of a single, isolated filament, or for a complete, (1G) superconductor (**Figure 3**), and in the very complicated conductor geometry shown in **Figures 4** and **15** for the 2G thin film, multilayer superconductor.

Needless to say, that the step from a single filament to highly diversified geometrical structures of the superconductor cross section means an enormous challenge to Finite Element calculations (in principle to all numerical methods). It becomes increasingly difficult to achieve convergence of the solutions. A new, tentatively applied, multiple repetitions Finite Element scheme (see later) finally had to be constructed, tested by trial and error, and applied to successfully achieve numerical convergence within tolerable computation times.

6.3. Radiation heat transfer in thin film superconductors (the small optical thickness case)

If thickness of a sample is small, like in case of thin films, and if also optical thickness is small (below about 10 to 15, see later for its justification), the Equation of Radiative Transfer (ERT) together with the Equation of Conservation of Energy (the “Energy Equation”, EQ) have to be solved: Omitting for simplicity a wavelength index, Λ , the ERT within the object under study reads [24], at a given time,

$$di'(\tau)/d\tau = -i'(\tau) + [(1 - \Omega) i'_{BB}(\tau) + \Omega/(4\pi) \int \Psi(\omega_i, \omega, \tau) i'(\tau) d\omega] (W/(m^2 \mu m sr)) \quad (12)$$

with i' the directional radiation intensity, τ the optical thickness, $d\tau = E ds$ (τ not to be confused with relaxation time), E the extinction coefficient, $E = A + S$, with A and S the absorption and scattering coefficients, ds a differential of the radiation path length, i'_{BB} the directional, black body (BB) intensity, $\Omega = S/E$ the Albedo of single scattering, and Ψ the scattering phase function. The quantities ω_i and ω indicate solid angles and apply to incident radiation (index i) and to the total unit sphere over which scattered and remitted radiation intensity has to be integrated. The term in square brackets denotes the “source function” (without the source function, Equations (12) and (14) reduce to the Lambert-Beer law when directional intensity, i' , is measured in transmission experiments in one direction only). It concerns absorption/emission and scattering light sources internal to the volume of the superconductor.

Once directional intensity, i' , now (as an extension of Beer’s laws) including the source term is obtained from Equations (12) or (14) and is integrated over the total solid angle to yield total radiation, q_{Rad} , the vector has to be inserted into the “Energy Equation”, namely Equation (13), the equation of conservation of energy. With q_{Cond} and q_{Rad} denoting the vector of solid conduction and radiative heat transfer, the energy equation reads using ρ and c_p for density and specific heat, respectively, of the sample material. Equation (13) yields the field of transient temperature distribution, $T(x,y,t)$, that now accounts for all relevant contributions to heat transfer (but additional contributions, if any become relevant, could easily be included). When this field is mapped onto the field of critical current density, the stability function Equations (1) and (2) can be calculated.

$$\rho c_p \partial T/\partial t = \text{div} (q_{Cond} + q_{Rad}) (W/m^3) \quad (13)$$

The above explanations presented for the problem heat transfer in general, and “radiative transfer” in particular, provide just a short summary of the principal solutions available for the complex heat transfer problem. In reality, the analysis of conductive and radiative transfer in thin films, especially in superconductor thin films, is much more complicated: This is because we also have to take into account preparation of the films and its impacts on conductive and radiative heat transfer.

In thin film superconductors, we roughly can distinguish three layers generated during film preparation (like evaporation, sputtering, or by chemical vapour deposition, CVD). We then have thin boundary layers each of about 100 to 150 nm thickness that in the simulations account for irregularities of the materials properties arising from substrate, superconductor thin film and stabiliser. While the solid/solid contacts can be modelled with random variations of electric and thermal transport parameters within the thin boundary layers against the superconductor thin film core, more complications arise in description of radiative transfer. We have investigated this problem in Sect. 4 [8]; just a short summary of how it can be solved shall be given here:

Consider a beam that is incident on the outer layer, ζ , of optical thickness, τ_ζ , of a thin superconductor film. While insertion of a term $(1 - R) A_\zeta i'(\tau = 0, t) \exp(-\tau_\zeta)$ into Equation (12), with $0 \leq R \leq 1$ the reflectivity, would describe attenuation of an incoming radiation beam, e.g. a laser at its particular wavelength, the attenuation by absorption (of radiation that is not reflected), within the thin boundary layer (or in a coating) of the superconductor, invariably initiates thermal, Black Body radiation and remission. Then we have to account in core of the superconductor thin films for the full Black Body spectrum, not only for just one wavelength (the wavelength of the incoming beam). A similar problem arises in the frequently cited Parker and Jenkins experiments [25] in which excitation of outer, here a normal or non-conducting layer, is initiated by an electron beam.

It is not clear that the outer layer, ζ , of the superconductor after deposition should have much stronger absorption properties (to become non-transparent at all wavelengths) than the interior of the 1.8 μm core; rather the contrary is to be expected: With thin (e.g. 100 to 150 nm) evaporated or sputtered or CVD thin surface films, homogeneity is not guaranteed, and extinction coefficients would be smaller.

It is obviously not helpful (and even is meaningless) to simply add to the ERT a term containing a factor $\exp(-\tau_{\zeta,\lambda})$, with Λ the wavelength of incident radiation, to account for absorption of *this* radiation in the thin surface layer and with *another* wavelength, Λ' , for propagation of radiation in the core and to look for closed form solutions of the ERT. The optical properties of the surface layer might too strongly be different from those of the core. Extension of the ERT, Equation (12), by an exponentially decreasing absorption term in which the term enclosed in curly brackets contains a wavelength, Λ' , different from the Λ of the core, cannot be integrated analytically,

$$di'_{\Lambda}(\tau_{\Lambda})/d\tau_{\Lambda} = -i'_{\Lambda}(\tau_{\Lambda}) + [(1 - \Omega_{\Lambda}) i'_{b,\Lambda}(\tau_{\Lambda}) + \Omega_{\Lambda}/(4\pi) \int \Phi(\omega_i, \omega, \tau_{\Lambda}) i'_{\Lambda}(\tau_{\Lambda}) d\omega] + \{(1 - R_{\zeta,\Lambda}) A_{\zeta,\Lambda} i'_{\Lambda}(\tau_{\zeta,\Lambda}) \exp(-\tau_{\zeta,\Lambda})\} \quad (14)$$

Instead, a procedure substantially different from standard radiation transport theory and from the Parker and Jenkins approached has to be found.

In a first step, a Monte Carlow approach to the exact solution (if a solution exists at all) serves for realizing this procedure. It concerns determination of the path lengths of photons during transition of a sample. This procedure immediately leads to a central problem of radiation heat transfer: Time dependence of the solution when scattering becomes important.

Scattering becomes important if the Albedo Ω is large. The Albedo of the YBaCuO 123 superconductor exceeds $\Omega = 0.8$ (decreases from about 0.94 to 0.8 within the temperature range between 92 and 91 K, respectively). Near the phase transition, scattering clearly exceeds absorption/remission. But scattering is a “fast” process in relation to absorption/remission, see below, **Figure 19** (and Figs. 11 and 12a [9]). Solutions of the ERT and of the EQ therefore have to be found in specific time intervals.

Extension of the single, standard ERT and Energy Equations to a “Matrix Method”, to cover also variations of parameters during simulation time and taking into account of in these time intervals the dominating wavelengths has recently been suggested [9], see below, Equation (16). Possible impacts on stability predictions would be important.

By its structure, the Matrix Method reflects “Discrete Ordinates” approximations [24,26], a type of quadrature formula (the Discrete Ordinates Method turns out as very successful in case there is strong anisotropic scattering).

The Matrix Method replaces the single Equations of (radiative) Transfer and of Energy Conservation by a system of transfer and energy equations. The ERT, Equation (12), is solved, roughly speaking, in a number of discrete directions, the “ordinates”, with the directions optimally selected, and the solutions are integrated over the solid angle to provide a corresponding system of energy equations.

In the Matrix Method, the scattering integral in Equation (12) is replaced by an expansion $\sum a_j f(\tau, \mu_j)$; in this expression, τ denotes optical thickness, μ_j are optimum directions and a_j are corresponding weights. In case only *one or two* directions have to be considered, the method reduces to the said “Two Flux Approximations” [24], if scattering is isotropic. Application of the Two Flux Approximation to a superconductor thin film has been reported in our previous papers, see the summary [13], Sect. 4. But the Matrix Method as suggested [9], in comparison to the discrete ordinate’s solutions, takes into account also the time and wavelength dependence of the conductive and radiative parameters, respectively.

In this approximation, the different heat transfer mechanisms are separated, in a matrix, M , line by line, according to the speed by which photons propagate through the superconductor (transit time through the sample depends on the number of interactions experienced by the photons¹²). Division into intervals separates “fast” from “slow” transport phenomena in radiation (scattering vs. absorption/remission), and in general, in multi-component heat transfer (solid conduction, radiation).

Figure 19 shows transition time of photons through the 2 μm thin film YBaCuO 123 superconductor, in dependence of temperature and for different absorption/remission and scattering situations.

By **Figure 19**, the sequence of equations in the Matrix formalism can be identified from **Figure 20**. For simplicity, the figure applies hemispherical spectral emissive Black Body radiative power to identify the sequence of intervals during warm-up of intervals between times $\theta_1, \theta_2, \theta_3, \dots$, like $\Delta\theta_{k,j} = \Delta\theta_{2,1} = \theta_2 - \theta_1$, all within the three regions that cover the surface layers, ζ , and the 1.8 μm core of the superconductor thin film. The Matrix Method thus separates time intervals, $\Delta\theta_{k,j}$ that are adjusted to the different transit times and corresponding values of the Albedo that are tested in **Figure 19**.

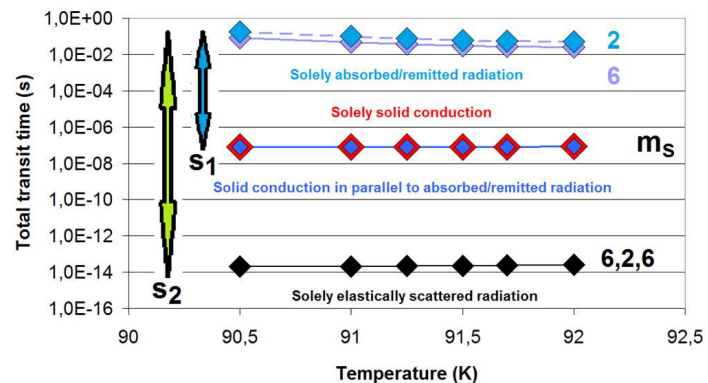


Figure 19. Transit time of solid conduction and radiation signals proceeding by different heat transfer mechanisms through the 2 μm YBaCuO 123 thin film. First published in arXiv 2111.09825 (Nov 2021), Figure 8b.

In **Figure 19**, we have simulated (1) solely absorbed/remitted radiation, (2) solely solid conduction, (3) solid conduction in parallel to absorbed/remitted (not scattered) radiation, (4) solely elastically scattered radiation. Cases (1) to (3) are calculated from

the diffusion approximation, see basic literature on heat transfer [27].

$$L = C (a_{Th} t)^{0.5} \tag{15}$$

if heat transfer is conductive (which in case of radiative heat transfer means: if optical thickness is large) and using anisotropy factors, m_s , indicated in the figure, and the Albedo Ω . Case (4) results from the Monte Carlo simulations. Time spans, s_1 , denotes time lag between two, fundamentally different, separate heat transfer mechanisms (solely solid conduction, radiation), s_2 is the maximum difference between two different, radiative transport processes.

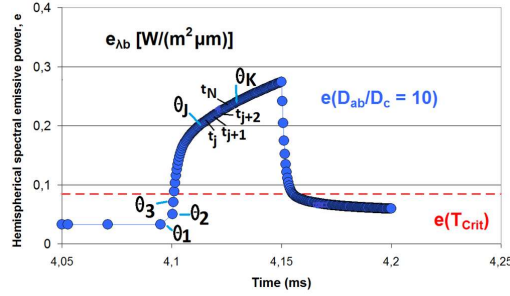


Figure 20. Hemispherical spectral emissive power, e_{lb} (solid blue circles, schematic), of Black Body radiation into vacuum. Reprinted from J. Supercond. Novel Magnetism 33 (2020) 3279–3311, Figure 9b.

In **Figure 20**, the e_{lb} are calculated using the Planck formula applied to temperature that increases with time in the superconductor under a short time disturbance. The dashed, horizontal red line indicates the e_{lb} that would be emitted at $T = T_{crit} = 92 K$ const. Times $\theta_1, \theta_2, \dots, \theta_J, \theta_K, \dots$ and their sub-divisions $t_1, t_2, \dots, t_j, t_{j+1}, t_{j+2}, \dots, t_N, t_{N+1}, \dots, t_{k-1}, t_k$ of each of the intervals $[\theta_J, \theta_K]$ indicate the intervals within which solution of the ERT, Equation (14), and the energy equation, Equation (13), shall be calculated by application of the Matrix method, Equation (16).

It is within *these* time intervals where solutions for the transport mechanisms under different wave lengths and parameters (Albedo, reflectivity, optical thickness) have to be found.

The matrix concept to solve the combined conduction plus radiative transfer problem, at every instant, t_i, t_j , (with two transfer mechanisms that operate in parallel) of course is laborious. But if the object under study is non-transparent, modelling of radiative transfer drastically simplifies to diffusion solutions (see Sect. 6.5), and the concept reveals an ideal condition for application of Monte Carlo (for radiative contributions) combined with Finite Element (for conduction heat flow) simulations.

A column vector, N , contains the corresponding energy equations. The Albedo in both M and N is selected in time intervals within which radiative or conductive transport mechanisms constitute (or both in parallel) contribute to total heat transfer by the matrix Equation (16),

$$\begin{pmatrix} \frac{dI(\tau)}{d\tau} = -I(\tau) + \Omega(4\pi) \int \Psi(\omega, \omega, \tau) I(\tau) d\omega, \Omega = 1 & 0 & 0 & 0 \\ 0 & \frac{dI(\tau)}{d\tau} = -I(\tau) + \Omega(4\pi) \int \Psi(\omega, \omega, \tau) I(\tau) d\omega, \Omega = 1 & 0 & 0 \\ 0 & 0 & \frac{dI(\tau)}{d\tau} = -I(\tau) + (1 - \Omega) I_{bb}(\tau) + \Omega(4\pi) \int \Psi(\omega, \omega, \tau) I(\tau) d\omega, \Omega < 1 & 0 \\ 0 & 0 & 0 & \frac{dI(\tau)}{d\tau} = -I(\tau) + I_{bb}(\tau), \Omega = 0 \end{pmatrix} \mathbf{X} \begin{pmatrix} \rho c_p \partial T / \partial t = \text{div}(\mathbf{q}_{\text{rad}}), \Omega = 1 \\ \rho c_p \partial T / \partial t = \text{div}(\mathbf{q}_{\text{SolidCond+eISc}}), \Omega = 1 \\ \rho c_p \partial T / \partial t = \text{div}(\mathbf{q}_{\text{SolidCond}} + \mathbf{q}_{\text{IneISc+AbsRem}}), \Omega < 1 \\ \rho c_p \partial T / \partial t = \text{div}(\mathbf{q}_{\text{SolidCond}} + \mathbf{q}_{\text{AbsRem}}), \Omega = 0 \end{pmatrix} = \begin{pmatrix} T_1 \\ T_2 \\ T_3 \\ T_4 \end{pmatrix} \tag{16}$$

Temperature is obtained in the results column vector, $T = M \times N$, by coupling matrix M with column vector N , like in a vector cross product of real matrix or column elements, to yield the temperature column elements, T . Elements (lines) of the Equation

of Radiative Transfer (contained in M) are folded with elements of the Energy Equation (arranged in N). The elements of M and N (all of which are equations, not just real numbers) for solution of the total heat transfer problem have to be applied with appropriate materials and boundary conditions. The method also allows considering spectral properties of refractive indices, Albedo and of the extinction coefficients.

This method to solve the combined conduction/radiation problem, in dependence of the speed by which energy transfer is realized, which means, within specific intervals of the simulation time, apparently has never been reported in the literature.

We will later present results obtained with Matrix and standard methods to solve the combined conduction plus radiation transfer problem in thin film superconductors. See arXiv 2102.05944 (Feb 2021), Figure 6a-c, for example.

The differences seen between both methods obtained for temperature excursion and stability functions apparently are small. It is not clear that small differences would result also from simulation of other materials (ceramics, metals, polymers). During numerical simulations, decisions must be made from comparison of e.g., actual (simulated) temperature, T , and superconductor critical temperature, T_{crit} . Both are given as real numbers, which means even tiny differences between both quantities, in a numerical quest, may lead to different decisions how to continue with the simulations (zero-loss or resistive current transport?). This far-reaching decisions, and similar ones, could lead to enormous differences in the simulations, following such quests. The Matrix Concept, accordingly, will have to be re-visited in near future.

The small differences, on the other hand, qualify both methods as suitable for investigating the impacts of parameter variations. This is reported below.

But how do we get the phase function in Equations (12) and (14)?

6.4. Monte Carlo method

Monte Carlo (MC) simulations yield the angular distribution of scattered radiation (the scattering phase function). This step is needed to also find realistic, efficient values of extinction coefficient (different from the result obtained in simple transmission measurements) and of optical thickness of the sample. The Monte Carlo simulation accordingly accounts for the integral, spatial distribution aspect of radiation energy within the combined parallel, conduction plus radiation heat transfer problem (**Figure 19**).

The Monte Carlo approach considers a large number M of beams that after emission experience a total N of interactions on their transit path of total length, L , through an object, like a superconductor filament or thin film (length, L , not necessarily equals sample thickness). Each beam shall be emitted from *any* position within a target area, at $z = 0$ and under arbitrary angles, θ , against the surface normal (“any position” means an extension of standard Monte Carlo simulations where it is assumed radiation is emitted from just one, single position; somehow unrealistic an assumption). Its transit time can be calculated for arbitrary events of absorption/remission and scattering interactions.

In the Monte Carlo language, beams are called “bundles”. For the general description of Monte Carlo simulations, when they are applied to radiative heat transfer [24].

The part $\Omega < 1$ (the Albedo) is responsible for the thermal energy remaining from the bundles after absorption/remission processes; this part is remitted or re-scattered (the case $\Omega = 1$ describes pure scattering, no absorption/remission events, no radiative equilibrium).

For the Monte Carlo method, the scattering angle, θ , under elastic scattering can be defined as a random variable to yield, as explained in a study [24], wherein $0 \leq R(\theta) \leq 1$, the probability to find a bundle emitted or scattered at angle θ (we have $0 \leq \theta \leq \pi$). Large m_s indicate strong forward scattering, compare the spider diagram in **Figure 17**,

$$\theta = \arccos [1 - R(\theta)/m_s] \quad (17)$$

In ceramic samples, the angular distributions of scattered radiation approach the better the theoretical $\cos(\theta)$ -distribution (when bundles leave the rear sample surface), the larger the extinction coefficient (and the larger the number of bundles).

All disturbances, here by absorption/remission, are the source of large numbers of radiation beams, first from foot-points in **Figure 16** at $(x > 0, z = 0)$ and, subsequently, of secondary beams after their absorption at random interior positions of the solid. The beams create internal heat sources, $Q_V(x > 0, z > 0, t)$. The Monte Carlo (MC) simulation yields spatial distribution and magnitude of these sources. More beams (in the language of Monte Carlo simulations: more bundles) are remitted from interior solid positions, $z > 0$, to create new sources, $Q_V(x > 0, z > 0, t)$, again simulated in the MC simulation.

After each absorption event along a bundle, the magnitude of the $Q_V(x, z, t)$ decreases until the bundle energy is completely extinguished. The total number of bundles in the Monte Carlo simulations performed in the present paper is $N = 5 \times 10^4$; this number proved to be sufficiently large in our calculations.

The scattering phase function, Ψ , in the superconductor materials is shown, first as the principal spider diagram in **Figure 17**, and explicitly for the YBaCuO 123 thin film material in **Figure 18**. When the scattering parameter, m_s , increases, scattering becomes increasingly forward oriented, but the spatial distribution of radiation leaving the rear surface, $y = L$, after multiple scattering interactions, finally reproduces the Lambert cosine law the better, the larger optical thickness, τ . A limit of $\tau = 15$, is found from experience. This can be concluded also from **Figure 21**.

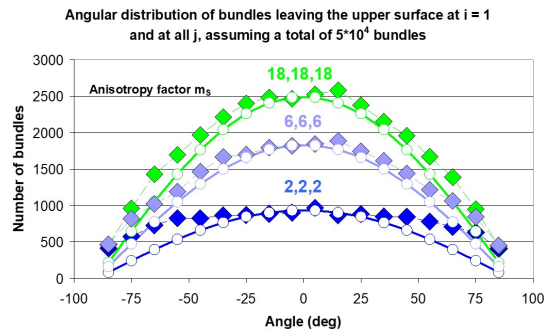


Figure 21. Angular distribution, $n(\theta)$, calculated at $2 \mu\text{m}$ thickness (coordinate $y = L$ in **Figure 16**) by Monte Carlo simulation of in total $M = 5 \times 10^4$ bundles. Reprinted from J. Supercond. Novel Magnetism 33 (2020) 3279–3311, Figure 16.

In this figure, the bundles are emerging from $y = 0$ (compare **Figure 16**) that leave the rear sample surface (thin film YBaCuO 123 superconductor). Results are shown vs. angle θ against surface normal of the volume elements (concentric rings generated by rotation of the area elements of **Figure 16**) and in dependence of the (scattering) anisotropy factor m_s . The curves (solid diamonds) are indexed as m_{S1}, m_{S2}, m_{S3} (running from 2 to 18; these are the same m_s that are applied in the spider diagram in **Figure 17** and the phase function (**Figure 18**). The m_s -factors in this figure are assumed as *identical* in inner (index 1) and outer, about $0.1 \mu\text{m}$ thin boundary layers (index 3) and in the 1.8

μm thick central core (index 2) of the thin film (for variations of the inner and outer layers see Figs. A2 and A3 [8]). The same applies to values of the Albedo ($\Omega = 0.912$ in the three layers, the value is taken from the study of Reiss [8]). Extinction coefficients in the three layers are $E_1 = E_3 = 3.417 \times 10^6$ and $E_2 = 1.409 \times 10^7$ 1/m, respectively [8]. Solid symbols approach the theoretical $\cos(\theta)$ -distribution (open circles) of the residual beams leaving the sample on the rear surface. The figure is copied from Figure A1 [8].

All items to determine the $Q_V(x, z, t)$, and the positions within the target plane from which bundles are emitted, in the MC simulation are treated as random variables.

According to a theorem by Carslaw and Jaeger [28], an initial distribution of sources, here radiative heat sources, is equivalent to a distribution of initial temperatures, to be taken into account for the solution of Fourier's differential equation (Sect. 6.5), here by the Finite Element method. This theorem provides another strong simplification of the combined conduction/radiation problem.

6.5. Optically thick superconductor samples

The criterion to reduce the general radiative transfer problem (previous Section) to a diffusion-like process, and to justify applicability of the so called "Additive Approximation" (see below) is given by the minimum optical thickness, $\tau = E s = 15$, of the sample [29] for justification of this condition; s denotes a distance within the sample, $s <$ sample thickness, D .

While it seems no problem to fulfil the condition $\tau \geq 15$ in direction of transport current flow, the y -direction in **Figures 3** and **4**, it is not clear this criterion will be satisfied also in the other directions in a filament or in a thin film. With their thickness in the order of 20 or only 2 μm , respectively, an extinction coefficient of the thin film material of at least $E = 7.5 \times 10^6$ (1/m) is requested, which might become a problem under dependent scattering.

If this approximation is allowed (if optical thickness is large), the integro-differential ERT, Equation (12) or Equation (14), reduce to a comparatively simple, second order (in terms of the spatial co-ordinate, x) differential equation, like Equation (10) or Equation (13). From the obtained, diffusion-like radiative heat flow, $q = q_{Rad}$, a "radiative conductivity", λ_{Rad} can be derived.

The radiative conductivity reads, after inclusion of a correction to anisotropic scattering to an effective value by the factor $\Omega\mu_m$, with μ_m the mean value of $\cos(\theta)$, θ as before the scattering angle, n the refractive index, and σ the Stefan-Boltzmann constant. See the study [30] for derivation of Equation (18).

$$\lambda_{Rad} = 16 \sigma n^2 T^3 / [3 E (1 - \Omega \mu_m)] \quad (18)$$

The radiative conductivity, λ_{Rad} , is added to λ_{Cond} . to yield total thermal conductivity, $\lambda = \lambda_{Cond} + \lambda_{Rad}$. This "Additive Approximation" of total thermal conductivity is not trivial, yet in good believe has it frequently been used in the literature. But its applicability was confirmed only recently in numerical experiments by the present author, see the study of Reiss [29], part A and B; (not really a surprise, it works only if optical thickness is large, which means λ_{Rad} is a small correction only, in the total conductivity, to λ_{Cond}).

The factor $\mu_m \Omega$ in the denominator of Equation (18), with μ_m a mean of the $\mu = \cos(\theta)$ directions, reduces extinction coefficient and optical thickness to effective values, which means the radiative contribution may significantly be increased by strong forward scattering and the diffusivity a_{Rad} accordingly increased.

6.6. Solid thermal and electrical conduction contribution

6.6.1. Heat transfer

If optical thickness is large, heat transfer in superconductors like in other solids is reduced to solid conduction. In our reports, we have applied solid thermal conductivity as temperature-dependent parameters obtained from experiments, the results either taken from the literature or, for thin films, determined in laser-flash or 3ω -measurements performed in the Department of Physics of the University of Wuerzburg.

6.6.2. Normal conduction, electrical resistances

Resistance under normal conduction is important for estimation of the flux flow resistivity, ρ_{FF} , arising in magnetic fields if, as mentioned, density of transport current exceeds critical current density. With the actual, local magnetic field induction, $B(x, y, t)$ used in the simulations, and $B_{Crit,2}$ the corresponding upper critical value of type II superconductors, the flux flow resistivity reads see Equation (7.10) by Huebener [1], with ρ_{NC} the normal conducting state resistivity. In the literature, Equation (19) has been used with ρ_{NC} still a uniform materials constant,

$$\rho_{FF}(x, y, t) = \rho_{NC} B(x, y, t)/B_{Crit,2} \quad (19)$$

For improved estimates of $\rho_{FF}(x, y, t)$, a more detailed value of ρ_{NC} in a cell model was designed [6] that reflects also the inner geometry and the materials composition of BSCCO 2223 multi-filament and YBaCuO 123 thin film conductors (**Figures 3 and 4**). The cell model in particular takes into account the microscopic, *layered* crystallographic structure of the BSCCO 2223 superconductor material (Fig. 2.13 of the study of Buckel and Kleiner [10]) and in particular the interfacial resistances (the weak-link problem in superconductors (while standard literature takes ρ_{NC} as just a continuum property of uniform value). All components of $\rho_{FF}(x, y, t)$ are treated as temperature-dependent quantities.

Design, and results obtained with the improved calculation of $\rho_{FF}(x, y, t)$ and the cell model are reported in **Figures 22 and 23**, respectively, showing how strongly $\rho_{FF}(x, y, t)$ increases with temperature and increasing magnetic field.

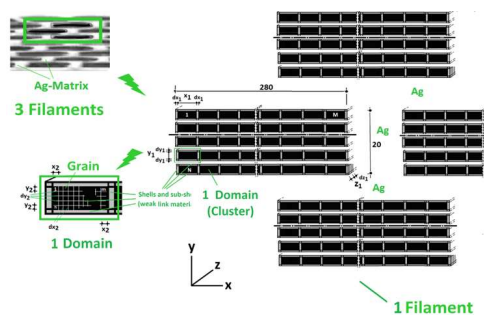


Figure 22. Geometrical cell model for the calculation of the resistivity, ρ_{NC} , for the estimate of the flux flow resistivity, ρ_{FF} , in the Finite Element simulations. Reprinted from J. Supercond. Novel Magnetism 29 (2016) 1405–1422, Figure 5a.

Figure 22, upper diagram to the left, shows three arbitrarily selected filaments (black, flat rectangles, schematic, not to scale. Circular cross sections could be modeled as well). Each filament (first detail, right, below) consists of a number $M \times N$ domains (clusters of orthorhombic plate-like, parallel oriented grains) each of which incorporate a superconductor core (large black rectangle) and a shell of weak link material (light-gray). Each of the $M \times N$ domains is divided into a number $N = m \times n$ grains (second detail,

bottom part of the figure, left) each with again a superconductor core (small black rectangles) and a thin sub-shell of weak link material (white lines); this hierarchy of large and small superconductor cores in domains and grains and of correspondingly thick and thin shells and sub-shells facilitates modeling resistances of grains and weak link materials of different size, thickness, materials composition, physical properties and field dependence, respectively. See caption to **Figure 22** for detailed positions of domains the corresponding weak links sections. Dimensions are given below, **Figure 23**. Total simulated conductor length, z , taken over large numbers of grains, domains and filaments is arbitrary. Numerical values indicating size of cross section of one filament are in micrometer. The geometrical model assumes roughly layered grains and filaments. Resistances to current flow, in this figure in y-direction, of all domains and grains, filaments and Ag-matrix material are switched in parallel. The multi-filament conductor in **Figure 3** incorporates 91 filaments.

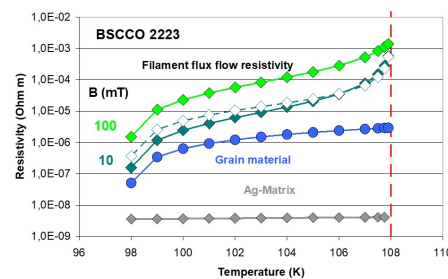


Figure 23. Flux flow resistivity, ρ_{FF} , calculated from the effective ρ_{eff} and with the field factor $B/B_{Crit,2}$ to current transport in a multi-filamentary BSCCO 2223 conductor. Reprinted from J. Supercond. Novel Magnetism 33 (2020) 629–660, Figure 17.

The calculations in **Figure 23** applied local (constant) magnetic flux density, $B = 10$ and 100 mT (solid dark-green and light-green diamonds, respectively). Dimensions of domains, x_1 , y_1 and z_1 , are 70, 6 and 70 μm , thicknesses dx_1 , dy_1 and dz_1 of weak link shells enclosing domains are 100, 10 and 100 nm, respectively (these are defined in **Figure 15**). Dimensions of grains, x_2 , y_2 and z_2 , are 20, 1 and 20 μm , thicknesses dx_2 , dy_2 and dz_2 of weak link shells surrounding grains are 1, 1 and 1 nm, respectively. Solid blue circles indicate ρ_{Grain} as solely the grain core (bulk) material without magnetic field and under zero current (note the temperature range reduced to $96 \leq T \leq 108$ K). Open dark green diamonds denote ρ_{FF} calculated with $B = 10$ mT. For comparison, dark-grey diamonds indicate resistivity of the Ag-matrix material. The upper critical magnetic field, at $T = 4.2$ K, is $B_{Crit,20} = 200$ T giving $B_{Crit,2}(T) = B_{Crit,20} [1 - (T/T_{Crit})^2]$. Critical temperature (vertical, dashed red line, for $B = 0$ and very small current) is 108 K.

In the BSCCO 2223 conductor, each of the filaments is embedded in a Ag-matrix to improve mechanical stability during winding and, as a normal conducting by-pass, to protect the conductor against quench.

6.7. The finite element model (description, results and achieved convergence)

6.7.1. Description of the FE model

In the previous Subsection we have shown that if radiation heat transfer can be simulated as a diffusion-like process, the solution of also the total heat transfer problem is enormously simplified, from the complicated Equations (12)–(14), and if they are

elements of the matrix equation, also from Equation (16), to the simple, 2nd order, Fourier’s differential Equation (10).

The solution can be found by analytical or Finite Differences or Finite Element (FE) methods (FE procedures would be preferred in case of complicated conductor architecture). Heat sources, $Q_0(x > 0, z = 0, t)$ and the $Q_V(x > 0, z > 0, t)$, are applied as input into a rigorous FE scheme to calculate thermalization of the sources and the transient temperature evolution $T(x, z, t)$, which in turn serves for determination of the field $J_{Crit}(x, z, t)$ of critical current densities of the superconductor and thus of the distribution of transport current. Mapping of the field $T(x, z, t)$ onto the field $J_{Crit}(x, z, t)$ is single-valued (injective) if there is no magnetic field.

Monte Carlo simulation to obtain the phase function is requested to correct extinction coefficients, E , to effective values, like in Equation (18) by the factor $(1 - \mu_m \Omega)$. Extinction coefficients are obtained from directional transmission measurements, or they can be calculated if complex refractive indices of the material are available in the appropriate range or wavelength. Also, the Albedo Ω should experimentally be determined of, like the extinction coefficient, calculated using methods described in traditional volumes on light scattering by small particles, for example Bohren and Huffman [31].

To obtain correct (converged) results of the excursion of $T(x, z, t)$ by the numerical FE integration of Equations (12) or (14) and (13), the whole simulated period in this and in our previous papers extended over up to 20 milliseconds (AC, one swing of 20 ms, $\omega = 50 \text{ Hz}$). It has been split into 200 equal length periods, sub-steps $\Delta t = 10^{-4} \text{ s}$. The procedure within each period Δt had to be repeated by up to $N = 10$ iterations (repetitions) of the proper (standard), one-turn integration loop in the FE process; this iterative repetition is indicated by the dark-yellow turn in **Figure 24**³.

Figures 24 schematically shows the “master scheme” for the FE-simulations, a flow diagram that explains the applied series of repeated, iterative Finite Element calculation steps. Predictions of the calculation steps and the saw tooth structure of the results are indicated in **Figure 25**, and the results confirming the predictions are found in **Figures 26** and **27**.

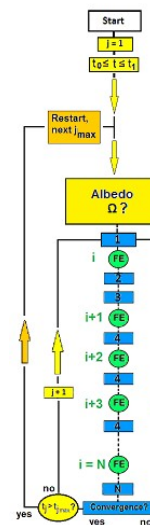


Figure 24. Flow chart (the “master scheme”) that has been used for an *extended* application of the Finite Element code Ansys Release 16.2 for simulation of the temperature fields. First published in arXiv 2212.09333 (Dec 2022), Figure 22a.

The master scheme shown in **Figure 24**, in strong contrast to traditional Finite Element procedures, incorporates two iteration cycles (i, j) and one time loop (t_j) of the numerical simulation. Light-green circles and indices, i : Sub-steps, the proper Finite Element (FE) calculations; Light-yellow indices, j : Load steps involving FE and, within the blue rectangles, critical current, magnetic field and resistance (flux flow, Ohmic) calculations; Dark-yellow arrow, t : Time loop, lines of a matrix M . The blue rectangles with sub-step numbers $i = 1, 2, 3, \dots, N$ are defined as 1: First FE step, j , with data input of start values of temperature distribution, specific resistances, critical parameters of J, B and of initial (uniform) transport current distribution or of single, isolated radiation heat pulses, respectively; 2: Results obtained after the first FE step (i), if converged, using identical parameters in the same load-step, j ; Calculation of $T_{Crit}, B_{Crit}, J_{Crit}$; 3: Calculation of resistance network and of transport current distribution (if applicable), all to be used as data input into the next FE calculation (sub-step $i + 1$), within the load step, j ; 4: Results like in 2; Sub-steps 5, 6, ..., N : Results like in 3 or 4, convergence yes or no? If “no”, return to 1 (iteration $i = 1$, in load step, j). If “yes” go to next load step $j + 1$, continue with 1. The number N of FE cycles (green circles) may strongly increase computation time. Length of simulation time, $t \leq t_{max}$, within each of the individual intervals, with t_{max} indicating the maximum time of a corresponding interval, is selected according to the different transit times (these result from Monte Carlo simulations, source functions, different radiation propagation mechanisms, different ratios of solid conduction and radiation, and from different wavelengths). After slight modifications (addition of the dark-yellow, outer time loop, the figure is copied from and extended against its original Figure 12 [29], part B.

Integration time δt within each sub-step $\Delta t/N \geq 10^{-5}$ s is between 10^{-14} and 10^{-7} s; convergence shall be achieved at the end of each sub-step, Δt and, finally, at the end of each period. Length Δt is large against, and safely contains, the three different characteristic times, $\tau_{Th}, \tau_m, \tau_C$, the items (i) to (iii) of Sect. 3.2 and in the Appendix.

This procedure considers the strong non-linearity of almost all involved parameters and transport processes. It yields a series of converged, quasi-stationary solutions. These are found in the “convergence circles” indicated in **Figures 25 and 27**.

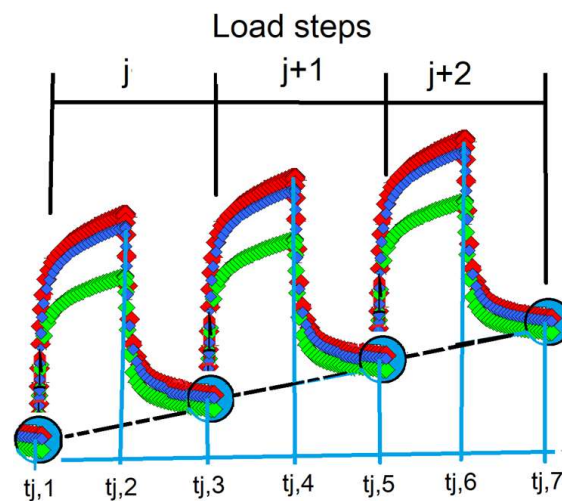


Figure 25. Prediction of “saw-tooth” behaviour of conductor temperature obtained as intermediate results during the iterations and the finally achieved convergence in the corresponding convergence circles.

The figure describes the Finite Element (FE) procedure integrated in the master scheme (**Figure 24**) using the code Ansys. Solution of Fourier’s differential equation, to calculate excursion with time of conductor temperature, $T(t)$, proceeds in the intervals Δt_j , $1 = t_{j,2} - t_{j,1}$ (disturbance, up-heating), $\Delta t_{j,2} = t_{j,3} - t_{j,2}$ (cool-down to convergence of temperature), ..., $\Delta t_{j,k} = t_{j,k+1} - t_{j,k}$ for given load-step, j ; we frequently observe $\Delta t_i < \Delta t_{i+1}$, depending on strength of the heat sources (not considered, for simplicity, in this figure). The dashed black line schematically indicates conductor temperature, $T(t)$, but may also indicate the T-dependence of any superconductor property like specific resistance, specific heat or thermal conductivity and may also indicate results of the analytical calculations (like J_{Crit} or the stability function) in the said master scheme. The black arrows schematically indicate the slow convergence behavior of the simulated temperature excursion with time. Convergence temperature (or, accordingly, convergence of any temperature-dependent property) then is obtained in the large, colored “convergence circles” (at the end of each load step wherein relaxation from the disturbance is obtained (the Finite Element solution cannot integrate the relaxation model)). The different colors applied to the diamonds schematically indicate different parameters by application of which the calculations will be performed, see captions to the figures shown in parts A and B of the study of Reiss [29].

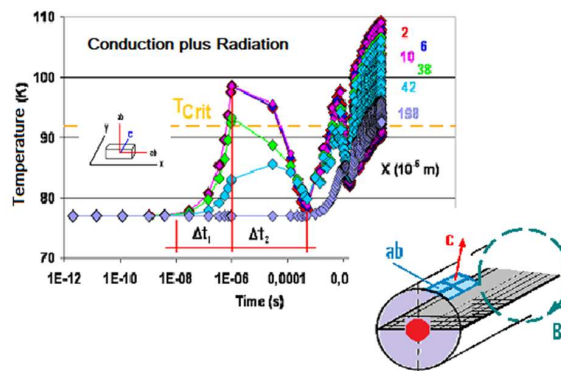


Figure 26. Verification of the predictions (by **Figure 25**): The “saw-tooth”-behaviour in a YBaCuO 123 filament of conductor temperature resulting from the FE simulations. Reprinted from J. Supercond. Novel Magnetism 33 (2020) 629–660, Figure 14.

Figure 26 shows element temperature under periodic point-like disturbance of DC transport in the thin filament of a 1G multi-filament conductor of 200 μm radius (The large radius is hypothetical and applies to filaments of this material prepared in the early days of HTSC development; actually, filament dimensions of (1G) BSCCO 2223 are much smaller, down to 20 μm .). The filaments were assumed as hypothetically being prepared from YBaCuO 123 poly-crystalline material (but BSCCO material meanwhile is preferred instead; it is only because more reliable YBaCuO 123 materials parameters were available at the date when this simulation was performed). Results are calculated with the c-axis solid thermal diffusivity parallel to the y-axis of the overall coordinate system. Orientation of orthotropic thermal diffusivity components of YBaCuO 123 with respect to the overall (x, y) coordinate system is shown in the inset positioned inside this figure, wherein the two thick, red solid lines assigned “ab” indicate direction of the (large) diffusivity in the crystallographic ab-planes, while the much smaller diffusivity component in YBaCuO is parallel to the c-axis. Results are given for solid conduction plus radiation thermal transport calculated at increasing radial distances, x , from the axis

of symmetry of one filament. The Δt_1 , Δt_2 reflect the two intervals of the integration scheme indicated for the first load-step. Because of the logarithmic plot, the following load steps cannot clearly be resolved in this figure. The horizontal, dashed yellow line indicates critical temperature (92 K) of this superconductor. The other inset, at right hand to this figure, shows the target positioned in the filament cross section. The ab-plane is rotated, and the dashed green curve denotes orientation of a circular magnetic field. The figure is re-plotted from Fig. 1a [6] and from Fig. 14 [29], part B.

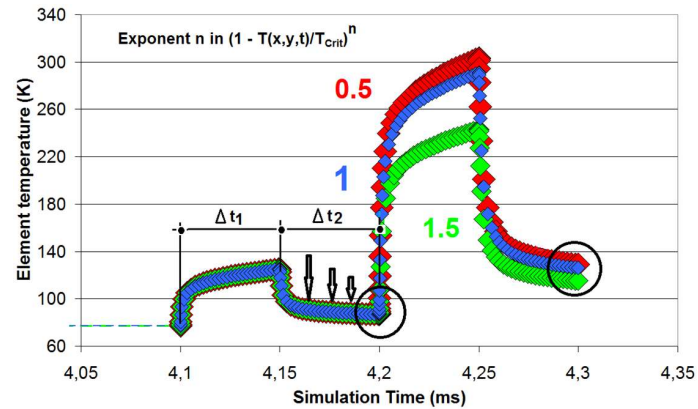


Figure 27. Verification of predictions (by **Figure 17**) of the “saw-tooth”-behaviour of conductor temperature.

Figure 27 shows conductor (centroid) temperature in the thin film, YBaCuO123 multi-layers during iterations in the “master scheme”, and black, open convergence circles at 4.2 and 4.3 ms. Excursion of conductor temperature, $T(x, y, t)$, proceeds in the intervals Δt_1 (disturbance, up-heating), Δt_2 (cool-down, relaxation); we have $\Delta t_1 \ll \Delta t_2$ ($T(x, y, t)$ decays exponentially). The length of the black arrows schematically indicates the (slow) slow convergence behavior of the simulated temperature excursion with time. Contrary to **Figure 26**, the temperature curve results from solely flux flow losses distributed in the superconducting conductor cross section (not from a pulse incident from outside onto the sample).

Radiation elastic scattering events, in the interior of the solid, proceed by velocity c/n of light (n the refractive index). But propagation of a thermal wave, by solid conduction only, is much slower, by orders of magnitude. Absorption and remission of radiation emanating from original positions ($x > 0, z = 0$) and by the $Q_V(x, z, t)$, at interior positions, accordingly, can be considered as *initial* conditions to the subsequently treated thermal conduction problem. This justifies application of the Carslaw and Jaeger theorem [28].

Thermalisation of the sources $Q_V(x, z, t)$ can be calculated using any standard, reliable FE program. Checking of the accuracy that they provide is recommended, e.g. by calculation of stagnation temperatures and of predictions that should be compared with experimental results, if available.

Thermal diffusivity and heat transfer to a coolant in the present calculations have been used as input values into the Finite Element simulation as temperature dependent quantities. While Rosseland mean extinction coefficients can be found in [24], see Equations (15)–(39) of this reference, to account for spectral variations of the extinction properties, the present analysis for simplicity is restricted to a constant extinction coefficient, E (independent of wavelength and temperature).

The Finite Element calculation step solves the differential part of the combined conduction plus radiation heat transfer problem. Accuracy of the FE method to a large extent relies on adequate meshing. Very fine, if possible, “esthetic” meshing using symmetries is helpful and required for the objects under study, filaments and thin films (not only the superconductor thin films in **Figure 4**).

Figures 28 and **29** show the Finite Element simulation cross sections (both schematic) of the (1G) multi-filamentary superconductor and of the (2G) multi-layer, coated thin film superconductor architecture (compare **Figures 3** and **4**, respectively).

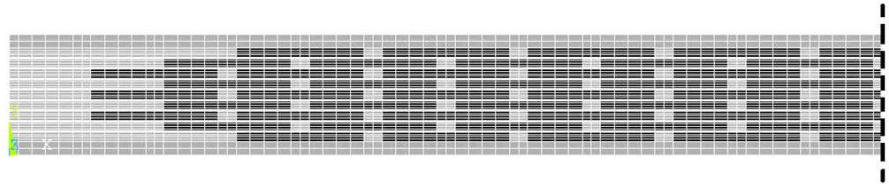


Figure 28. Finite Element simulation scheme of the left half of the BSCCO 2223 conductor cross section. Reprinted from J. Supercond. Novel Magnetism 29 (2016) 1405–1422, Figure 3 (lower diagram).

Figure 28 schematically shows the 91 identical superconductor filaments (black) and matrix material (Ag, light gray). The thick dashed line at the right denotes axis of symmetry, $x = 1.92$ mm. Thin white lines indicate details of the finite element, mapped meshing (with a total number of elements $N_{El} = 4032$). In this conductor, and if there a heat pulse is applied to test stability of this conductor, a “target” would preferentially be positioned onto the cross section of one or of a few of the filaments to initialize heat flow in axial, y-direction (compare **Figure 26**). Otherwise, the heat sources (flux flow, Ohmic) result from too large a transport current and are located within the filaments.

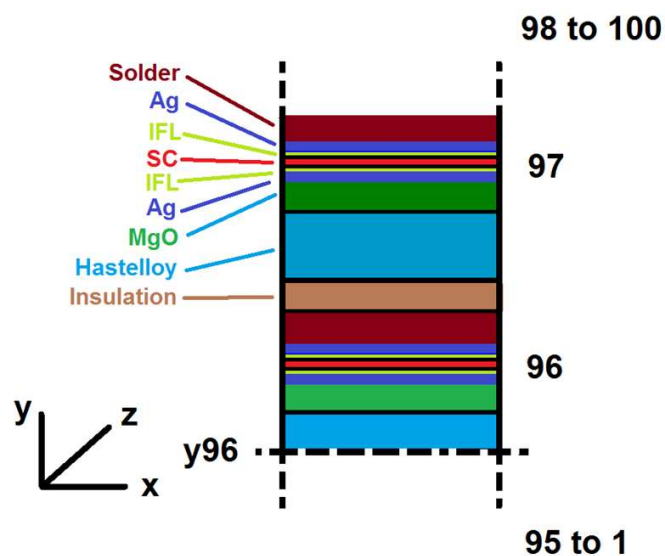


Figure 29. Finite Element simulation scheme of coil and of (2G) YBaCuO 1223 conductor geometry. First published in arXiv 2111.09825 (Nov 2021), Figure 1.

The figure shows in detail the composition of turns 96 and 97 of the coil (**Figure 15**, again schematic, not to scale). This figure, contrary to continuum approximations, is used for detailed specifications of the numerical stability calculations. Crystallographic c-axis of the YBaCuO-layers is parallel to y-axis of the co-ordinate system. Conductor

architecture and dimensions are standard. Superconductor (SC) layer thickness (red sections) is 2 μm , its width 6 mm; thickness; these data apply to also thickness and width of the Ag elements (lilac); width of the interfacial layers (IFL, light green) is 40 nm (the IFL are included to simulate surface roughness and diffusion of species between the SC and its neighbouring Ag- and MgO-layers, respectively). The thick, dashed-dotted line at the bottom of this diagram indicates an artificial axis of vertical symmetry introduced for support of the Finite Element part of the simulations, compare text for explanation. While continuum approximations, like those reported in the 7th International Workshop on Numerical Modelling of High Temperature Superconductors (HTS 2020), enormously simplify simulations of temperature excursions in superconductor applications, they like other continuum models cannot yield temporal and spatial resolution. But highly resolved simulations are the prerequisite to development of superconductors and to identify onset and expected location of a quench.

Total number N_{EI} of elements in the half cross sample sections applied to the (1G) multi-filamentary superconductor was 1440, 4032 and 12384. Though it yields overall agreement with integral results that were obtained with larger numbers of elements (total transport current, distribution of hot spots, stability functions), the $N_{EI} = 1440$ mesh resolution turned out to be too coarse for a detailed study of temperature distribution. $N_{EI} = 4032$, found by trial and error, probably is the smallest number that can be tolerated for simulation of transient problems in this complicated conductor geometry (and $N_{EI} = 4032$ still is an economical measure).

For the cross section of the (2G) thin film superconductor cable with its upper 5 turns, N_{EI} had to be increased strongly, up to 64,000 in total.

The simulations apply mapped meshing of the cross sections using 4-node plane elements, temperature dependent materials properties and boundary conditions.

Computation time became very critical and almost impractical on a standard PC (4-core processor) when using $N_{EI} > 10^4$. Total simulated period had to be limited to about $t \leq 12.5$ ms. It took about 26 hrs to simulate this period in the simulation of 1G and 2G superconductor samples.

The solution scheme applies sparse matrix, direct solves, with appropriate definition of the number of equilibrium iterations. The FE processes are embedded into the already mentioned, overall, 4-level calculation scheme (**Figure 24**). Application of iterative solvers did not substantially improve the situation.

Resistance to magnetic transport has to be considered separately in grains and in grain boundaries. A schematic, rather optimistic, c-axis orientation of plate-like grains that constitute the filaments, and a circumferential magnetic field, under axial (y -) direction of transport current, is assumed. Flux flow, under this condition, would occur in horizontal (x, y -) directions (under c-axis orientation of superconductor grains, within the crystallographic ab-plane; strictly speaking, current transport in the ab-plane is larger (may be larger even by orders of magnitude) against c-axis direction, because of large anisotropy ratios).

Like in our previous reports, we have used data for solid/liquid heat transfer from metallic surfaces to boiling LN_2 , including its dependency on temperature and circumferential position.

Results obtained for both superconductors are shown in **Figures 30** and **31**, respectively.

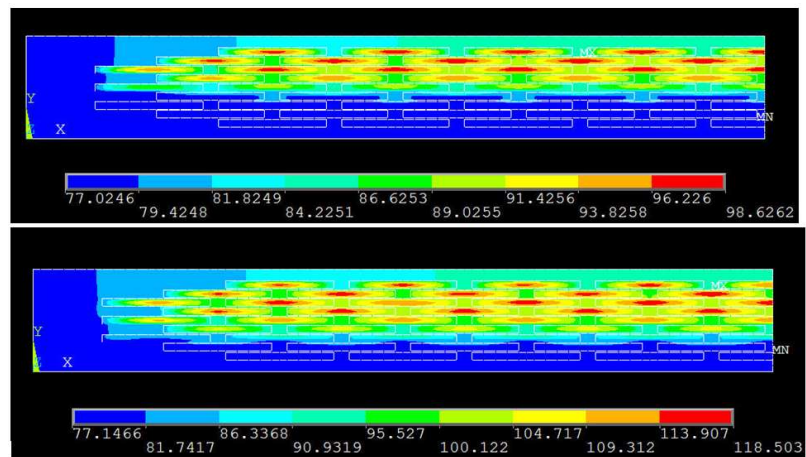


Figure 30. Temperature field (nodal temperatures) in the tape cross section of the BSCCO 2223 multi-filamentary conductor (**Figures 3** and **28**) obtained in a FE calculation. First published in arXiv 2102.05944 (Feb 2021), Figure 15b,c.

In **Figure 30**, again because of symmetry, only the left half of total conductor cross section needs to be shown, and the symmetry axis is on the right. Results are observed at $t = 8.3$ ms (top, with all temperatures, $77.0246 \leq T \leq 98.6262$ K, below critical temperature, $T_{Crit} = 108$ K at zero magnetic field), and at $t = 8.6$ ms (bottom), respectively (1.8 and 2.1 ms after start of a permanent disturbance initiated by a large fault current). Resistances according to the bottom (temperature) diagram partially are Ohmic, but are mixed with flux flow resistances as can be expected from **Figure 5** (mid diagram). The disturbance results from a sudden increase, within 2.5 ms, beginning at $t = 6.5$ ms after start of the simulations, of AC transport current to a multiple of 20 times its nominal value. Local temperatures are identified by the corresponding horizontal bars below the diagrams. Symbols MX and MN indicate positions in the cross section where minimum and maximum temperature is observed. Temperature in the upper half of both diagrams is larger than in their lower half cross sections; in this example of field orientation, magnetic flux density arising at the Ag/filament interfaces in the upper half cross section is settled to exceed flux density in the corresponding lower half sections, which by reduction of J_{Crit} initiates non-zero flux flow resistances in the (upper) regions. Transport and fault over-currents thus preferentially occupy the lower half of the cross sections. Even temperature distributions within the tiny filaments, not only over the total tape cross section, can be observed in both diagrams.

Figure 31 shows finally achieved numerical convergence of the results obtained during the temperature simulations in the cross section (**Figure 4**) of the multilayer, thin film conductor. An additional, but small heat source (a trigger), is approximated by incidence of a short radiation pulse, Q_0 ($x > 0, z = 0, t$), but only on the solid red circle on the upper conductor surface in **Figure 4**. The target plane ($z = 0$) in this case is located on the flat surface of the superconductor (i.e. on the crystallographic ab-plane, with favorable c-axis orientation of the sample).

The solution is cylindrical symmetry. Its convergence is demonstrated by comparison of conductor temperature at its periphery (i.e. at “cold spots” within the conductor) with temperature of the coolant ($T = 77.0000$ K) and by control of stagnation temperature at all positions of the conductor after a disturbance.

Coolant temperature is the only temperature that must remain absolutely constant, strictly at 77 K, at the very interface between coolant and solid (this is a boundary

condition, kept constant during the whole simulated period). A sharp criterion for convergence is to find exactly this temperature at positions within the conductor but very close to the interface, under the enormous geometrical thickness differences, layered samples, strongly different materials and their strongly different, anisotropic thermal and electrical transport properties. That this condition has been fulfilled in the FE simulations is a favourable result that confirms the applied numerical method.

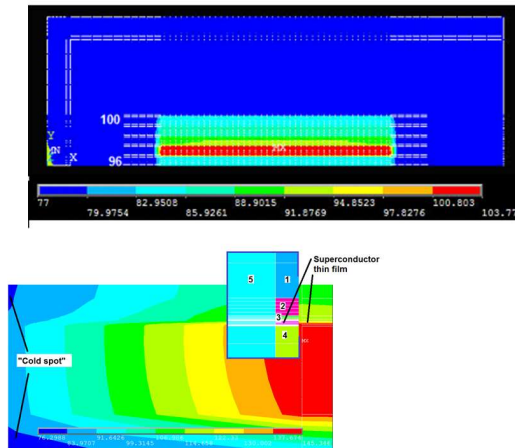


Figure 31. Verification of numerical convergence when using the procedure explained in **Figures 24** and **25**. First published in arXiv 2111.09825 (Nov 2021), Figure 11c.

In its upper diagram, **Figure 31** shows nodal temperature distribution within the conductor cross section (turns 96 to 100) in the coated YBaCuO 123 conductors at $t = 4.1$ ms after start of the simulations. Coated, thin film conductors using YBaCuO 123 are preferentially applied in energy technology. White dashed lines are part of the Finite Element mesh (the inner block comprises turns 96 to 100 of the coil; the narrowly spaced double, dashed white lines indicate electrical insulation between turns, and the outer double lines reflect reinforcement of the casting compound). Again, symbols “MX” and “MN” denote maximum and minimum temperature within the total conductor cross section. Numerical convergence of the simulation is confirmed by exact reproduction of the temperature minimum, 77.0000 K (coolant temperature, pool boiling) in both cases. Lower diagram: Nodal temperature distribution between turns 96 and 100. Temperature, here shown at $t = 4.27$ ms, has increased against $t = 4.2$ ms. No fault, just nominal transport current, $I_{Transp}/I_{Crit} = 1$. Below, the strongly magnified section (inset) shows temperature distribution at the left end of the superconductor thin film in turn 96 with a “Cold spot” arising during the iterations. The inset identifies materials and their positions and their temperature within the conductor cross section around turn 96: 1 Stabilizer Cu, 2 PbSnAg-solder, 3 metallization Ag, followed by interfacial layer Ag/SC, superconductor (SC) thin film, interfacial layer SC/Buffer layer, 4 buffer layer MgO, 5 Hastelloy.

In the simulations, we have applied random critical superconductor parameters (see **Figures 32** and **33**), with fluctuations of critical temperature, current density, magnetic field, weak link behaviour, as a method to (i) approximately account for deficiencies (unavoidable, on industrial scale) in materials development, manufacture, handling and operation of the sensitive 1G conductor (micro-pores and cracks that result from winding).

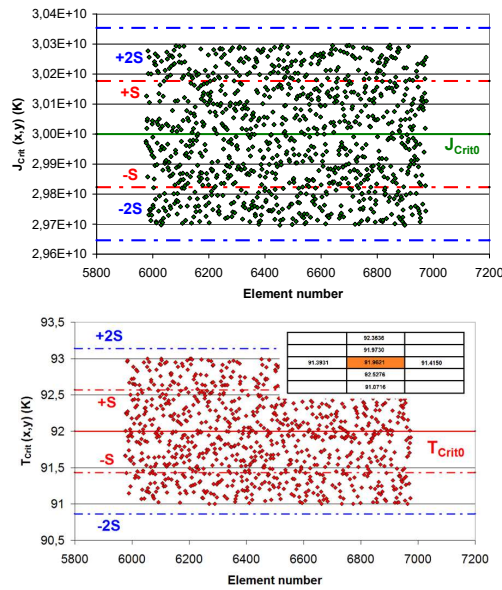


Figure 32. Random variations of ΔJ_{Crit0} of critical current density (upper diagram) and of the thermodynamic variable, ΔT_{Crit0} , of critical temperature (below). First published in arXiv 2111.09825 (Nov 2021), Figure 2.

The variations ΔJ_{Crit0} in this figure within 1 per cent around the mean (thin film) value $J_{Crit0} = 3 \times 10^{10}$ A/m² of YBaCuO 123 in zero magnetic field and at $T = 77$ K, the variations ΔT_{Crit0} are within 1 K around the mean value $T_{Crit0} = 92$ K in zero magnetic field. In the lower diagram, the inset shows element temperatures in the immediate neighbourhood of the centroid of turn 96 (orange rectangle). Solid green and red lines indicate mean values, blue and red, dashed-dotted lines are mean-square deviations. In both diagrams, random variations and their mean-square deviations are the start point for subsequent, overall variations of these parameters in that multiples of these are used in the simulations. Nodal distances in horizontal and vertical directions in the superconductor thin films are 30 and 0.4 μ m, respectively. These random variations applied in the numerical stability calculations accordingly modify the standard “existence of superconductivity diagram” (see traditional volumes on superconductivity).

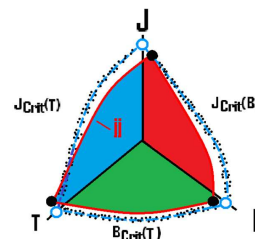


Figure 33. Existence diagram of type II superconductivity (schematic, not to scale; the lower critical magnetic field is not shown). The diagram indicates variations of the thermodynamic variables T and B and of the variable J. Reprinted from J. Supercond. Novel Magnetism 31 (2018) 959–979, Figure 8.

The dashed blue line and the open blue circles in this figure denote the conventional region of existence of superconductivity (the open blue circles accordingly are located on the corresponding axes of the diagram). Random variations of $T_{Crit}(B)$, $J_{Crit}(B)$ and $J_{Crit}(T)$ against this (conventional) region are indicated by small black dots; this applies

(schematically) to the existence diagrams of all elements in the Finite Element scheme. The random variations (**Figure 32**, taken as standard variations in each of the area elements) ΔT_{Crit} , $\Delta B_{Crit,2}$ and ΔJ_{Crit} of the electrical/magnetic critical parameters against the conventional values of YBaCuO 123 in the present paper are within ± 1 K, ± 5 Tesla and ± 1 per cent, respectively. For a particular element number, jj , as an example, its region of superconductivity existence is indicated by the coloured quadrants that in this single, special case are (exaggerated) located all *within* the conventional region (the dashed blue curves). Thick black solid circles indicate for this element the critical values T_{Crit} , B_{Crit} , J_{Crit} that, again exaggerated, are shifted against the conventional values.

A second justification for using randomly scattered critical parameters (against mean values) shall be mentioned: (ii) Standard theory of superconductivity interprets phase transitions from superconducting to normal conducting states as events that sharply (strictly speaking: idealistically) proceed, which means how (by which steps, or how quickly) the corresponding limits like T_{Crit} are exceeded. But the transition of sample temperature above critical temperature, $T > T_{Crit}$ sharp, hardly can be controlled in practice. Instead, interpretation of T_{Crit} as a randomly (but within tight limits) fluctuating parameter relaxes the comparison from idealistic to a realistic conditions.

Further, (iii) during the simulations of transient temperature fields, $T(x,y,t)$, the computer permanently checks the condition $T(x,y,t) > T_{Crit}(x,y,t)$ “yes or no”, in order to decide whether to continue the simulation with “superconducting or normal conducting state of the sample”. The decision “yes” might lead to prediction of hot spots or even of quench. The point is: Even tiny differences between $T(x,y,t)$ and $T_{Crit}(x,y,t)$ at constant time, t , are sufficient to corrupt the decision (note that both $T(x,y,t)$ and $T_{Crit}(x,y,t)$ are real numbers, in the strict mathematical sense). The variations indicated in **Figures 32** and **33** are expected to compensate such corruptions, on a statistical basis.

By a very large number of elements, trivially the *average* of the random distributions of J_{Crit0} , T_{Crit0} and B_{Crit20} almost perfectly coincides with their physical (standard) values. But in reality, a number of local values of J_{Crit} , T_{Crit} and B_{Crit2} possibly might diverge from the uncertainty (percentage) range in **Figure 32**. A specific value $T(x, y, t) > T_{Crit}(x, y, t)$ again might initialize development of a hot spot at the temporal position (x, y, t) even if the stability function, $\Phi(t)$, Equations (1) and (2), remains below $\Phi(t) = 1$ (a sample calculation is reported, see later in **Figure 36**). In other words, the stability function, $\Phi(t) < 1$, an integral value taken over the total conductor cross section, does *not* guarantee that no hot spot would be generated. Control of local conductor temperature, if $\Phi(t)$ closely approaches $\Phi(t) = 1$, would become inevitable.

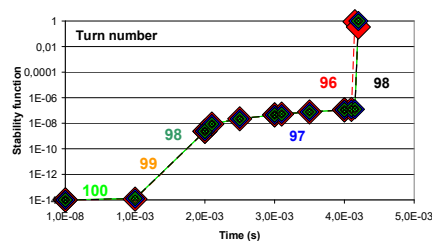


Figure 34. Stability function, $\Phi(t)$, obtained for solid conduction plus radiation heat transfer (and solid/liquid heat transfer at the solid/coolant contacts) in the thin film, YBaCuO 123 superconductor. Reprinted from J. Supercond. Novel Magnetism 33 (2020) 3279–3311, Figure 5a.

Results are shown for turns 96 to 100 (for the numeration see Fig. 4a [13]) of the

coated conductor winded to a coil. The calculations assume a sudden increase of transport current above its nominal value beginning at $t = 3$ ms; flux flow resistances then are responsible for thermal losses that locally increase conductor temperature. All curves in this and in the following figures apply “standard” uncertainties ΔT_{Crit} , $\Delta B_{Crit,2}$, ΔJ_{Crit} and the anisotropy factor, Δr (within ± 1 K, ± 5 Tesla, ± 1 per cent and ± 0.5 , respectively) of the *electrical/magnetic* critical parameters T_{Crit} , $B_{Crit,2}$ and J_{Crit} (92 K, 240 Tesla and 3×10^{10} A/m² at $T = 77$ K) and of the anisotropy factor ($r = 10$, again at $T = 77$ K) of the thermal diffusivity, as in previous papers (see text and **Figure 32** for explanation of the uncertainties). Uncertainties of solid thermal conductivity, λ_{Cond} , and of critical current density, J_{Crit} , in the following tests are superimposed on the results achieved with the “standard” set (see Captions to the corresponding figures). In the present figure, coloured curves are obtained with *no* random fluctuations of λ_{Cond} , and of J_{Crit} , but the black crosses instead apply to a ± 5 per cent random variation of λ_{Cond} , at randomly selected positions within turn 98.

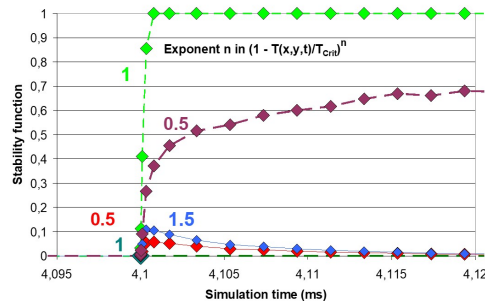


Figure 35. Stability function, $\Phi(t)$, of the YBaCuO 123 thin film superconductor (showing details near $t = 4.1$ ms). First published in arXiv 2111.09825 (Nov 2021), Figure 9a.

The figure considers elements of turn 96 (dark-brown diamonds). By its steep increase of $\Phi(t)$ at $t = 4.1$ ms, the figure clearly identifies the onset of a first quench. No fault current, just nominal transport current, $I_{Transp}/I_{Crit} = 1$. The calculations apply different values n of the exponent in the relation $J_{Crit}(x, y, t) = J_{Crit0}(x, y, t_0) [1 - T(x, y, t)/T_{Crit}]^n$. In this figure, critical current density J_{Crit0} is considered as *uniform*, $J_{Crit0} = 3 \times 10^{10}$ A/m² at 77 K in all elements, but of course, $J_{Crit}(x, y, t) = J_{Crit0} (1 - T/T_{Crit})^n$, and without the other statistical fluctuations. Resistive current limiting is provided, apparently almost completely, by turn 96 (light-green and dark-brown diamonds). At $t > 4.115$ ms, zero loss transport current would decrease by about 30 per cent when instead of $n = 1$ (light green) the value of the exponent n is reduced to 0.5 (dark-brown diamonds).

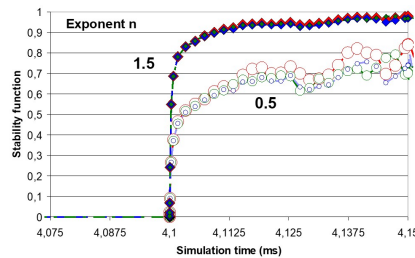


Figure 36. Stability function, $\Phi(t)$, of the YBaCuO 123 thin film superconductor (detail near $t = 4.1$ ms) of the YBaCuO 123 thin film superconductor (all elements of turn 96). First published in arXiv 2111.09825 (Nov 2021), Figure 9b.

The figure compares results obtained with application of $T_{Crit} = T_{Crit0}$ uniform and $T_{Crit} = T_{Crit}(x, y, t)$. No fault, just nominal transport current. Like in **Figure 34**, onset of the quench is clearly identified from the sudden increase of $\Phi(t)$ at $t = 4.1$ ms. Results are obtained with values $n = 1.5$ (solid diamonds) and 0.5 (open circles) of the exponent in the relation $J_{Crit}(x, y, t) = J_{Crit}(x, y, t) [1 - T(x, y, t)/T_{Crit}]^n$, for constant ratio $X = D_{ab}/D_c = 5$ of the thermal diffusivity and for $I_{Transp}/I_{Crit} = 1$. Also, critical current density J_{Crit0} is uniform, $J_{Crit0} = 3 \times 10^{10}$ A/m² at 77 K in all elements. For the decision whether the superconductor is in zero loss, flux flow or Ohmic states, the calculation compares $T(x, y, t)$ with locally different values $T_{Crit}(x, y, t)$ under variations within the maximum spacing ΔT_{Crit0} . Red, blue and green symbols denote results obtained with differences and ratios (i) $T(x, y, t) - T_{Crit0}$ and $T(x, y, t)/T_{Crit0}$, (ii) $T(x, y, t) - T_{Crit}(x, y, t)$ and $T(x, y, t)/T_{Crit}(x, y, t)$ and (iii), $T(x, y, t) - T_{Crit}(x, y, t)$ and $T(x, y, t)/T_{Crit}(x, y, t)$, respectively; the differences in $\Phi(t)$ are greater if $n = 0.5$. At values of $\Phi > 0.7$, zero loss transport current would decrease by about 20 per cent when instead of $n = 1.5$ the value $n = 0.5$ is applied. Differences among results obtained with options (i) to (iii) at $t > 4.14$ ms (open circles), though below 15 per cent, cannot be neglected, which means item (iii) has to be considered for reliable stability calculations.

However, temperature measurement hardly can be taken at the surface of filaments or thin films (and we do not know position of a hot spot before it is encircled closely by numerical simulations, like the one reported in **Figure 37**). The experiments suggested in Sect. 7 of the paper would become applicable for also this case. Permanent supervision, by detection of minute variations of electrical field over the conductor during warm-up, is a practical solution.

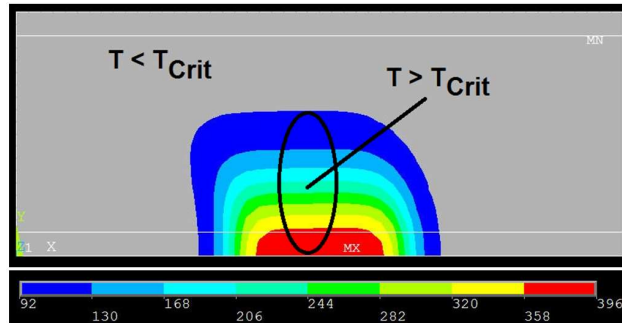


Figure 37. Encircling position and growth of a quench. The figure is copied from a presentation by the author at the 7th International Workshop on Numerical Modelling of High Temperature Superconductors (HTSmod 2020). First published in arXiv 2102.05944 (Feb 2021), Figure 5b.

In **Figure 37**, the temperature distribution under solid conduction plus radiation in the $2 \mu\text{m}$ YBaCuO thin film, is obtained for a strong, rectangular heat pulse of in total $Q = 2 \times 10^{-9}$ Ws applied to the target during $0 \leq t \leq 8 \times 10^{-9}$ s. Simulation time is 5×10^{-8} s. Temperature of a considerable part of the superconductor cross section exceeds T_{Crit} . Zero-loss current transport then is possible only within the shaded (grey) area.

The Meissner effect is checked separately in each of the finite area and volume elements of the numerical calculation scheme.

The problem emerging from the crystallographic anisotropy in both YBaCuO 123 and BSCCO 2223 superconductors, frequently expressed by the ratio of thermal diffusivity, $X = D_{ab}/D_c$ in ab-plane and c-directions, becomes obvious in their electrical and thermal transport properties and in penetration depth of magnetic fields. The

anisotropies are strongly different in different orientations of the crystallographic axes. In the YBaCuO 123 material, we have the anisotropy ratio, X of up to 20, in BSCCO 2223, X is even larger, by at least an order of magnitude, and the anisotropy of current transport accordingly is comparably large.

Anisotropy may constitute serious problems to Finite Element simulations. Further, we have to treat a variety of temperature-dependent transport parameters, and there are in addition the cooling interactions (solid/solid conductive, convective and pool boiling) that sensitively depend on temperature differences between solid surface and coolant (this dependence is frequently neglected in the literature or has not been seen at all).

Results obtained with additional, but as well important parameter tests are presented in **Figures 38** and **39** (in contrast to **Figures 32** and **33**: not of only statistical fluctuations of superconductor thermodynamic critical parameters but, in addition, of given, fixed variations of thermal conductivity and of critical current density, and their impact on temperature excursions and stability functions). Differences seen between results obtained when using the Matrix Method, Equation (16), or the standard, traditional method, Equations (12) or (14) and (13) obtained so far were small, at least in the superconducting thin films. But even very small differences may corrupt decisions on how simulations of the physics behind (super- or normal conducting states) continue with on-going time. More simulations are necessary (and will be reported in a subsequent paper).

In summary, the small differences presently observed between both methods (Matrix or traditional method) last not least confirm that in general, the approach to investigate superconductor stability by numerical simulations, is successfully confirmed. However, the complicated stability problem, as has become clear from the preceding Sections of this paper, needs more numerical investigations.

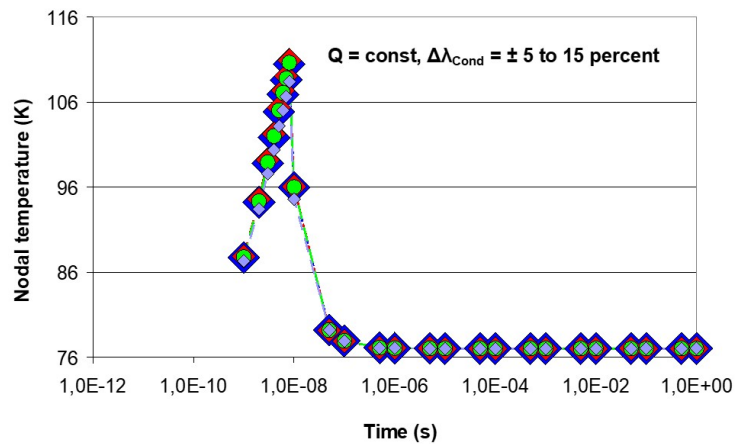


Figure 38. Nodal temperature, $T(x,y,t)$ (coloured diamonds), obtained at $z = 0$ in the centre of the target at constant incident power (a rectangular heat pulse of in total $Q = M 1.25 \cdot 10^{-12}$ Ws, here using the factor $M = 5$, applied at $t \geq 0$ onto the circular target of duration 8 ns). Reprinted from J. Supercond. Novel Magnetism 33 (2020) 3279–3311, Figure 15a.

In **Figure 38**, results are shown for the levels $i = 1$ to 5, thin layers of $0.1 \mu\text{m}$ thickness (counted from the surface into the “depth” of the conductor). Then continue with Fig. 6, part b and c [8], for details. Temperature (under adiabatic conditions) is obtained for conduction plus radiation (diffusive) heat transfer and random fluctuations,

$\Delta\lambda_{Cond}$. The fluctuations possibly interfere with random fluctuations, ΔJ_{Crit} , within ± 1 per cent of critical current density that were simulated in this figure. For more details, see the description of Fig. 7a [8].

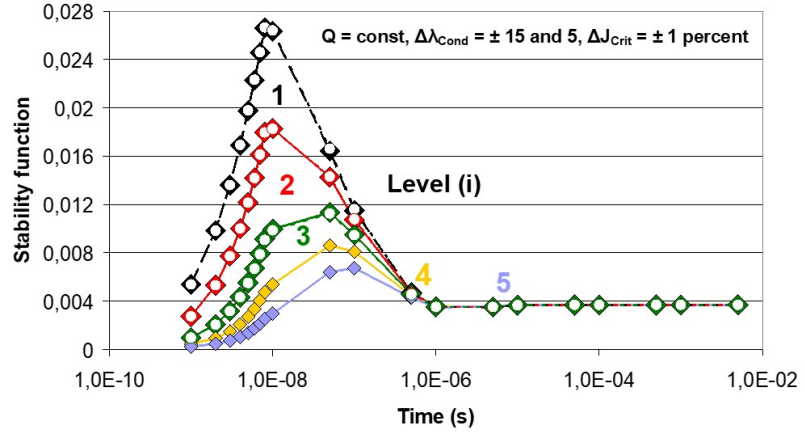


Figure 39. Stability function, $\Phi(t)$, calculated from Equations (1) and (2).

In this figure, a rectangular heat pulse of in total $Q = M \times 1.25 \times 10^{-12}$ Js, using $M = 5$, is incident on the target ($z = 0$, starting at $t \geq 0$) during in total 8 ns. Results using the temperature distribution in **Figure 38** are shown for the levels $i = 1$ to 5 of the Finite Elements schemes (again, thin layers of $0.1 \mu\text{m}$ thickness, see Figure 6 [29], part b for explanation of “levels”). Results are shown for adiabatic conditions and conduction plus radiation (diffusive) heat transfer. The calculations assume random fluctuations, $\Delta\lambda_{Cond}$, within ± 15 in the elements of level 1 and within ± 5 per cent in level 2, of the solid thermal conductivity, λ_{Cond} (solid diamonds). Open circles denote fluctuation of $\pm 5\%$ of λ_{Cond} in the elements of both levels $i = 1$ and 2. The fluctuations possibly interfere with those arising from random fluctuations, ΔJ_{Crit} , within $\pm 1\%$ of critical current density, J_{Crit} (the uncertainty ΔJ_{Crit}).

6.7.2. Summary of the Finite Element simulations

As the result of the Finite Element simulations, **Figures 5, 6, 27, 30** and **31** have shown the temperature fields in the (1G) multi-filamentary tape and in the (2G) thin film cross section at different times after start of the simulations (the conductor geometry was shown in **Figures 3** and **4**). Losses are due to a large AC fault current beginning at $t = 6.5$ ms after start of the simulations that within 2.5 ms in this simulation is assumed to increase by a multiple of 20 times its nominal value. In other words, losses in superconductors not necessarily arise only in case of local incident heat pulses, absorption of radiations or by insufficient cooling, but it is the flux flow losses that also have to be taken into account.

Finally, **Figures 27** (by the obtained temperature distribution), and **Figures 34-36** (by the stability functions) identify onset, and **Figure 37** also the position of the onset of a quench, at few milliseconds after start of the simulations.

What remains to be shown is existence of the second critical temperature, T_{Quench} (see below, Sect. 7 of the paper).

The prediction of a probably existing, second critical temperature that might result from incomplete relaxation is in line with problems experienced when in the early days of high temperature superconductor development, J_{Crit} -measurements in some laboratories were performed with analogue currents. This procedure resulted in a

hysteresis-like excursion of the electrical field, like the one observed in **Figure 40** (its upper part): Voltage detected over 1G multifilament BSCCO samples was not identical under increasing or decreasing probing current [32]). Later, the apparent hysteresis was avoided when the analogue, continuously increasing probing current was replaced by short (3 ms) current pulses (lower part of **Figure 40**).

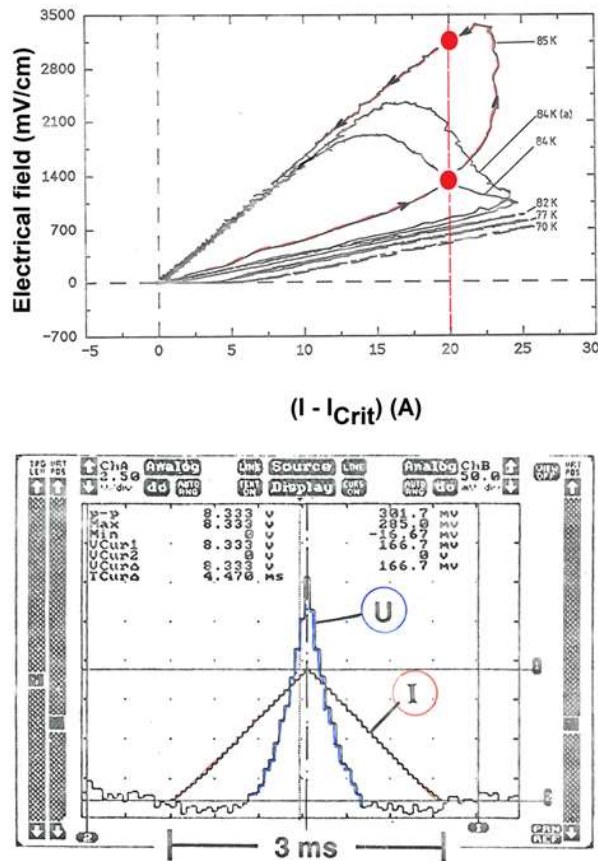


Figure 40. Electrical field measured over a YBaCuO sample either with continuously increasing probing current (upper diagram) or using a short current pulse, I (below).

In the upper diagram of **Figure 40**, the solid red circles are introduced by the present author to highlight the strongly different voltages detected when a continuously increasing/decreasing probing current is applied to the sample to determine critical current from onset of a resistance. Both diagrams, with slight modifications by the present author, are copied from internal reports of the ABB Research Centre, Heidelberg (unpublished). The reports applied results obtained in a Diploma Thesis [32] prepared by Fitzer under the auspices of Prof. W. Jutzi, University of Karlsruhe, Karlsruhe (Germany). Under short pulses, the energy supplied to the sample was too small to lead to substantial temperature increase that trivially would have reduced J_{Crit} and thus increased resistance of the sample. This was the intuitive explanation¹⁴ but the electron system probably had not been given enough time for completion of relaxation during the continuous increase of probing current (the disturbance initiated by $J > J_{Crit}$). This expectation is not contradicted by the lower part of this Figure (the field E vs. time triangle). The short pulse avoids generation of a thermal disturbance extended in time and magnitude. Experiments are suggested in the following to clarify the situation.

7. Concepts to confirm Impact of Relaxation on J_{Crit} and on Observables $X(J_{Crit})$

The Meissner effect relies on generation of screening currents to provide magnetisation that expels an external magnetic field from the interior of a superconductor sample. Screening currents, like all currents within a superconductor, flow with critical current density. Control of levitation height, Z , over sufficiently long periods of time, the clearest manifestation of the Meissner effect, thus would reveal completion of relaxation, which means: When levitation height, Z , finally is constant.

The excursion of $Z(t)$ with time accordingly has to be measured with great precision. Measurement of observables $X[J_{Crit}(t_{Eq})]$, here $Z(t_{Eq})$, can be performed with existing optical devices with little technical adjustments.

This also applies to measurements of any other observable that depends on J_{Crit} .

For the success of the levitation experiment, any undesired variation of $Z(t)$ of a superconducting sample positioned above an array of magnets, or of a magnetic sample above superconductors, that might result from e.g. convection in the coolant or from condensation of water vapour on the corresponding sample (if it would leave the coolant) has to be excluded. The experiment therefore has to be performed in vacuum, with cooling solely by radiation exchange with cryogenically cooled walls of a super-insulated vacuum vessel. After completion of cool-down of the sample to coolant temperature, the experiment should be continued under variable sample temperature (below critical) in order to generate disturbances by an auxiliary heater.

The point is: Temperature should, after an initial experiment, in the following not be kept constant but the experiment would be performed under variable, preferentially increasing temperature, by application of heat pulses, or even under oscillating temperature starting with low and continued with increasing frequency (the latter performed in order to check whether relaxation can quickly enough can follow the temperature variations and be completed or not within given time intervals). Care has to be taken to define the range of frequencies, to avoid absorption (and possible collisions with ESR), and to avoid hysteresis losses.

From the results obtained for levitation, the maximum acceptable uncertainty in $Z(t)$ near T_{Crit} can be estimated from Fig. 7a–f [13] when several thermal interactions in parallel between sample and its environment is taken into account (not just trivial a task; interested readers are invited to discuss this with the author).

Further, it would be very interesting to see how relaxation exerts impacts on attractive forces between normal and superconductor samples in magnetic field, like in a cryogenically cooled, Cavendish gravitation balance (with m_1 magnets, m_2 superconductor samples). In the gravitation balance, the difference between magnetic repulsion and gravitational force would be controlled.

In comparison to measurement of levitation height, planning and realisation of these experiments has the advantage that suitable experimental devices already exist that need only technical adjustment. Again, these experiments have to be performed in vacuum and data should be taken under variable temperature, with the devices super-insulated against thermal losses.

Another option would apply a super-insulated cryogenically cooled, magnetic suspension balance operated in vacuum, with m_1 a strong magnet and m_2 a superconductor sample hanging above the mass m_1 , and using a heater to realise temperature variations around a level close to the phase transition. Instead of levitation

height, levitation force, strictly speaking, the difference between levitation force and sample weight, has to be measured, as is schematically indicated in **Figure 41**. It is easier, and yields more reliable results, to control zero force difference (which would be observed in the equilibrium state) than measuring absolute values.

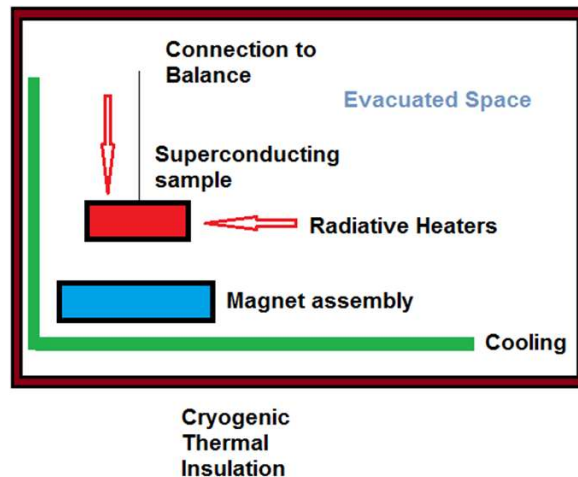


Figure 41. Proposed set-up of an experiment (schematic) to control levitation force, F_{lev} , after disturbances imposed by radiative heating of the sample after cool-down.

An interesting variation of the experimental set-up has been shown in Figure 2 of the study of Riise et al. [33]. While the reported modelling of the proper levitation process is convincing, the experiment is performed with the sample cooled by LN₂ in open atmosphere and assuming stationary, constant temperature conditions. But it is not clear there will be no disturbances of the measurement caused by the boiling liquid and by condensation of water, oxygen or nitrogen vapour on samples and magnets.

The experiments should also yield the number of normal conducting, single electrons, at temperature near but below T_{Crit} , by in parallel performed electron spin resonance (ESR) measurements. This number, but not all, may originate from decay of a previously existing, thermodynamic equilibrium state. They only temporarily, within relaxation time, contribute to the total number of normal conducting electrons. The higher the temperature, the larger is this number. Since the number of decay products is very small against all normal conducting electrons (because the number of electron pairs is comparably large as long as $T \ll T_{Crit}$), their contribution to the ESR-signal might be tiny.

8. Summary and outlook

As overall conclusion, we note that numerical simulation of the stability problem, by its high spatial and temporal resolution, is superior to continuum approximations (like uniform conductor temperature or homogeneous materials composition), and is superior also to analytical methods and worst-case conditions, in short: It is superior in relation to all existing traditional, analytical stability models.

These results have been reported by the present author since 2012. From these results, the following has been derived as corollary since June 2023 and is reported in the present paper. In particular, we have shown, first for practical consequences, that Numerical (Finite Element) solution of Fourier's Differential Equation are by far superior to standard stability models; the numerical solution allows to encircle with

precision the location of the source of a quench (a hot spot), or the quench itself, in filamentary and thin film superconductors. It identifies the time after start of a disturbance when it is no longer possible to block its excursion.

In theoretical aspects, we have found that in strict mathematical interpretation, T_{Crit} , can be considered the limes of a series of non-equilibrium states, which means T_{Crit} cannot be considered as the equilibrium value of a physical observable (i.e. cannot be understood as a uniquely, sharply defined thermodynamic quantity), and that a second “critical temperature”, T_{Quench} , as the *onset* of a quench (and of the onset of the thermal phase transition, as a local hot spot), can be identified; it may be interpreted as a “temperature or state of no return” that contrary to the standard T_{Crit} is observable: It is the first state that shows non-zero resistance during sample warm-up.

When inspecting very closely J_{Crit} , not a sharp, instantaneous break down of critical current density will be expected when the superconductor approaches its phase transitions. J_{Crit} is not switched off suddenly and completely at a hypothetically existing, critical temperature, but is reduced continuously when instead the temperature T_{Quench} is exceeded. This proceeds mostly within short time intervals that, however, asymptotically diverge near the phase transition.

Approximately fulfilled linear correlation between superconductor critical current density and density of electron pairs, together with numerically confirmed linear correlation between entropy and relaxation time, extends the spectrum of available tools to protect superconductor stability. Besides control of voltage over the sample (the traditional tool), also control of temperature T_{Quench} , of relaxation time, of density of electron pairs or of single electrons, and of J_{Crit} (sharp break-down or continuous break-down within minute periods of time?) can be mentioned as alternatives.

Calculation of entropy differences between initial and final states (after completion of the relaxation process) confirms that the expected decrease of entropy really is the driving force for relaxation. The driving force increases the stronger the more temperature approaches the phase transition.

These conclusions result from the presented integral, Multiphysics view of the quench process. It comprises elementary properties of many-particle systems (analogies to nuclear physics exploited in the microscopic stability model), thermodynamic considerations (temperature uniquely defined under solely thermal equilibrium, after completion of relaxation), relaxation of the superconductor from excited states back to electron pair formation, standard heat transfer principles (solid conduction in filaments plus radiation propagation in filaments or thin films, temperature-dependent heat transfer to coolant).

All these steps have been considered to realize the multi-physics investigation of the superconductor stability problem. This is not “new physics”.

Development of a modified version of relaxation model to calculate relaxation time also for decay of spin-lattice correlations in paramagnetic substances, or for electron/hole transitions in semi-conductors at same or different momentum states, or for nuclear spin correlations, would be a challenging future task.

Declaration: With the exception of **Figures 3 and 4** (see Citation in the Figure Captions), all figures and results reported in this review paper (numerical simulations and experimental data) are elements of lectures “Applied Superconductivity” given by the author at the University of Wuerzburg, Dept. of Physics, Wuerzburg, Germany, or the results were obtained during experiments performed in the laboratory of the Author's

Research Team at the Asea Brown Boveri (ABB) Research Center, Heidelberg, Germany. **Figures 5, 6, 26, 27, 30, 31, 37, 38, and 39** have been calculated by me using the Finite Element code Ansys purchased from Cadfem GmbH, Munich (Germany). No figures were copied from other work.

Conflict of interest: The author declares no conflict of interest.

Notes

1. In a type II superconductor, at temperature below critical temperature, an external magnetic field will create single or an array of magnetic flux quanta in the superconductor material if the field exceeds the lower critical field of this material. The flux quanta usually are “pinned” locally, e.g. by microscopic inhomogeneity of the material that by pinning forces keep their positions locally stable. But under a transport current, flux quanta become subject to Lorentz forces, and if current density exceeds critical current density, the Lorentz force may exceed pinning force and get part or the whole array of the quanta into current-induced motion. Therefore, a voltage is induced over the sample that indicates an electrical resistance, the “flux flow resistance, ρ_{FF} (Ωm), with corresponding “flux flow losses” if current is not re-distributed or switched off. Compare Equation (7.10) in the book of Huebener [1].
2. The sets comprise: (a) Normal conducting electrons, the overwhelming number of electrons residing deeply in the Fermi Sea, (b) electron pairs in the ground state of the superconductor; these consist of single but correlated electrons that without quantum-mechanical principles like the Pauli principle “initially”, as single particles, would fill the energy gap, but are shifted to the upper and lower edges of the energy gap (the dark-blue shaded areas in **Figure 1(a)**); according to standard BCS-theory, these electrons together with regular, normal conducting electrons (the light-green sections) constitute the source for generation of electron pairs, (c) excited electrons resulting from decay of electron pairs under disturbances, in a simplified view either if the decay energy is large enough to lift them over the energy gap, or if they run against and statistically penetrate this barrier, (d) excited electrons called “quasi-particles” (we will come back to this item in Sect. 4 during calculation of entropy production), (e) the ionic lattice of the superconductor material (as it interacts with single electrons or quasi-particles), (f) phonons, excitations of the lattice, that as exchange Bosons (spin one particles) provide binding (correlation) of single electrons to pairs, and serve as thermal energy transport quanta, (g) photons (mid IR) that enhance solid conduction (phononic) thermal energy transport.
3. This conclusion is misleading and would provide only a qualitative method to determine relaxation time. While the authors [10], too, consider states outside thermodynamic equilibrium, their model does not consider decay of previously excited states and their recombination to pairs and the selection rules by which recombination (relaxation) has to be realized. And two more arguments shall be given here: (i) Electrons injected into the superconductor Al, as in the experiments reported by Gray et al. [34,35] are indistinguishable. For comparison, let a few N spheres be added to a system of an already existing number, M . If during injection, both N and M , in the total entity $N + M$, are indistinguishable (like electrons as Fermi particles), can these be separated during relaxation into the original N and M ? No. Separation can be realized correctly only if N and M can be selected according to a new selection criterion (finding this criterion in case of the spheres might become difficult). In case of electron injection, however, this means the selection for the relaxation process must be realised with respect to angular momentum (the Pauli principle), and to their addition rules that have to be fulfilled for recombination of two electrons to an electron pair. The single electrons forming a pair are continuously replaced by others (one might better speak of electron correlations to form pairs instead of once forever selected electrons to constitute the pair). The selection rules are not restricted to the number N (such a limitation would introduce a method to distinguish the N from the M particles). As a consequence, electrons after their injection, for realizing relaxation, have to be selected from the whole electron body, $M + N$, not only from the number N of injected particles, contrary to the study [10], and the selection process has to be performed stepwise, in strict successive order, otherwise the Pauli principle would be violated; (ii) When, for example, people are displaced, it takes the longer to reunite them the larger this number and the smaller the number of remaining partners (if the total number is constant). In case of electrons, this means the number of “displaced” electrons, N , resulting from decay of pairs, increases with increasing temperature, and selection of potential (remaining) “partners” from M (again, if the total number is constant), for each of the N , has to be initialized for more and more individual N . Accordingly, with decreasing temperature, the solid curve indicating relaxation time decreases with decreasing, and diverges

- with increasing temperature. The model [11] in contrast to the study [10] provides a method to quantitatively, at least in principle, though only in an approximation, determine relaxation time after disturbances.
4. Starting with two single electrons that by decay of a pair have been excited to energy levels above the energy gap, their re-condensation to pairs, in logical order of the relaxation process, has to realize the sequence: (i) First, identification of potential partners (other single electrons), the identification performed by one electron of these two, that are “suitable” (allowed by selection rules) for re-condensation to a pair, (ii) the proper re-condensation process (binding, better addressed as: “correlation” of two electrons to a pair), and (iii) re-location of the pair to the top of the Fermi Sea (positioned at the Fermi level in the energy diagram). The question is how this sequence can be described not only in terms of energy (like in Figure 1a) but also in terms of temperature. This immediately leads to the central problem raised in this paper: (a) Why at all, (b) at which time after decay and (c) at which temperature should the decay electrons recombine to electron pairs? How can the temperature of the pairs be defined? See the discussion of these items in Sect. 4 where we consider entropy production during the relaxation process. The idea pursued in this paper was to circumvent most of the complications by just counting, stepwise, electron by electron, the number of open repair channels” (partners available for pairing), and since each of the minute, single repair steps would request a very small-time interval for its realization, they finally must be summed up to total relaxation time. Total relaxation time (see **Figure 4(a)**) immediately leads to the problem of how to define temperature during the relaxation process and temperature of its result.
 5. In the Deuteron, the only stable bound, two-particle nucleon system, we have a central binding force (plus a small electrical quadrupole moment) and a comparatively small binding energy so that the inter-particle distance between proton and neutron even exceeds the range of the nucleon/nucleon interaction force. In the BCS-model, it is sufficient that there is a (negative) binding energy that even may be arbitrarily small. Formation of both a nucleonic bound state, like in the Deuteron, and of an electron bound state (the electron pair) proceeds within a time interval (the time of flight, or lifetime that the corresponding exchange Boson (π or ω , respectively) needs to mediate the binding interaction (or correlate the corresponding single particles before recombination). The analogy therefore comprises: (1) In the Yukawa model, time of flight of the mediating Pion determines the uncertainty of the size of the nucleon (or the lifetime of two uncoupled nucleons before they combine to a nucleon-nucleon pair in a nucleus); (2) In the electron pair, time of flight of the mediating Boson determines the uncertainty of the size of the electron pair (or the lifetime of two excited states before they recombine to an electron pair in a superconductor). The uncertainty of the size of the electron pair is the average “distance” between the two particles concerned. In both cases, dividing this distance by the velocity of the corresponding exchange Boson, $d(t)/v$, which provides a measure for the “lifetime of the interaction” and, if appropriately summed up over all particles concerned, the intrinsic part of the “lifetime of the disturbance”, $\tau = \tau_{EI}$ (to be identified with the term $\partial c(x, t)/\partial t$ in Equation (4) [11]). There are of course differences between the three cases considered (nucleon-nucleon interaction, Deuteron and electron pair) [11]. But electron pair formation, i.e. (i) a two-particle interaction, (ii) a Boson (the phonon ω) as the (virtual) exchange particle and (iii) a weakly bond, two-particle states, get the electron pair in superconductors, though only from formal aspects, at least marginally similar to its nucleon/nucleon analogue.
 6. An example is exponential damping of temperature during propagation into depth under daily and annual variations of incident solar energy. A similar case arises in combustion motor construction when after ignition of the combustion gas/air mixture a thermal wave penetrates the motor cylinder linings, at high frequency.
 7. An amusing, but correct, informative interpretation of “quasi-particles” given by Mattuck [36] has become well-known in the literature: A single particle moving through a system of others (of same type, and through the ion lattice) “pushes or pulls on the particles in its neighborhood and becomes surrounded by a cloud of agitated particles similar to the dust cloud kicked up by a galloping horse in a western (the real particle plus its cloud constitutes the quasi-particle, and the particle cloud screens the real particle.” Mattuck concludes: The quasi-particle can be treated as approximately independent of the others, and quasi-particles resemble the real particles quite closely.
 8. In Equation (20.16) of the study of Falk and Ruppel [16], because of $p = N k/V$ in ideal gases, the temperature T cancels (k is the Stefan/Boltzmann constant). The system (electron pairs plus single, including decay electrons) is not a thermodynamically closed system, since it is subject to disturbances, like warm-up due to flux flow losses from fault currents. In a closed system, entropy increases under irreversible processes, like decay of electron pairs. Only processes, in which the entropy increases, run by themselves, which settles direction of all processes (Clausius principle). However, the present system is open to disturbances (like fault currents), is not left to its own, is not a closed thermodynamic system. A Gibbs

thermodynamic system (by its changes, dE), is stable the more its energy and entropy attain minimum and maximum values, respectively. This is reflected in Figure 12.

9. The Fermi-Dirac distribution function has to be applied (excited electrons are spin $\frac{1}{2}$ particles): If $D_{E,p}$ indicates population density, D_E the (available) density of states and F_E the Fermi distribution function (the occupancy number, $F_E = 1/(\exp(E - E_F) + 1)$), then $D_{E,p} = D_E F_E$. A Boltzmann factor could be applied in the simulations to find density and occupation of energy levels above the energy gap (but $E - E_F$ in the given temperature range is not very large compared to kT).
10. It is most probably not a spurious correlation, from solely physical reasons: Any transport current density increases with increasing charge carrier density. The more charge carriers (electron pairs in superconductors) contribute to current transport, the larger is the density J_{Crit} below which no zero-loss current transport becomes possible. Compare definition of the stability function, Equations (1) and (2).
11. In an analogue thermophysical model designed by the author, the diffusivity of highly excited nuclear matter was successfully determined.
12. Besides Figures 10a and 12a and 13a [9] that show transit time of mid-IR photons through a thin film, YBaCuO 123 superconductor for different values of the Albedo, $\Omega = 0$ (absorption/remission) or Ω close to 1 (pure scattering that proceeds with the speed of light), the number of interactions has been calculated by Monte Carlo simulation (Figures 8 and 9 [8]). Since transit time for the different Ω differs by order of magnitudes, solution of the radiative, and of the total heat transfer problem must be found in clearly different time intervals, with correspondingly detailed ERT and EQ given by the elements of matrix M and column N .
13. This is clearly an unconventional extension of standard FE procedures that rely on only a single integration loop, but the extension has turned out to be necessary to obtain convergence in view of the strong non-linearity of almost all involved materials and transport parameters.
14. Originally, this observation was interpreted as resulting from heating-up the sample by transport current greater than critical current density generating flux flow resistance below standard critical temperature (a temperature increase would increase overall resistance and electrical field over the sample). But the result shown in **Figure 40** instead might originate from incomplete relaxation, which means, critical current density was smaller than its equilibrium value.

References

1. Huebener RP. Magnetic Flux Structures in Superconductors. Springer Berlin Heidelberg; 1979. doi: 10.1007/978-3-662-02305-1
2. Kadin AM. Spatial Structure of the Cooper Pair. Journal of Superconductivity and Novel Magnetism. 2007; 20(4): 285-292. doi: 10.1007/s10948-006-0198-z
3. Wilson MN. Superconducting magnets. In: Scurlock RG (editor). Monographs on cryogenics. Oxford University Press; 1989.
4. Dresner L. Stability of superconductors. In: Wolf St (editor). Selected topics in superconductivity. Plenum Press; 1995.
5. Cardwell DA, Larbalestier DC, Braginski AI. Handbook of Superconductivity. CRC Press; 2022. doi: 10.1201/9781003139638
6. Reiss H. Finite Element Simulation of Temperature and Current Distribution in a Superconductor, and a Cell Model for Flux Flow Resistivity—Interim Results. Journal of Superconductivity and Novel Magnetism. 2016; 29(6): 1405-1422. doi: 10.1007/s10948-016-3492-4
7. Reiss H. Inhomogeneous Temperature Fields, Current Distribution, Stability and Heat Transfer in Superconductor 1G multi-filaments. Journal of Superconductivity and Novel Magnetism. 2016; 29(6): 1449-1465. doi: 10.1007/s10948-016-3418-1
8. Reiss H. Stability of a (2G) Coated, Thin-Film YBaCuO 123 Superconductor: Intermediate Summary. Journal of Superconductivity and Novel Magnetism. 2020; 33(11): 3279-3311. doi: 10.1007/s10948-020-05590-3
9. Reiss H. An attempt to improve understanding of the physics behind superconductor phase transitions and stability. Cryogenics. 2022; 124: 103325. doi: 10.1016/j.cryogenics.2021.103325
10. Buckel W, Kleiner R. Superconductivity. Published online January 2004. doi: 10.1002/9783527618507
11. Reiss H. A Microscopic Model of Superconductor Stability. Journal of Superconductivity and Novel Magnetism. 2012; 26(3): 593-617. doi: 10.1007/s10948-012-1800-1
12. Reiss H. Stability Considerations Using a Microscopic Stability Model Applied to a 2G Thin Film Coated Superconductor. Journal of Superconductivity and Novel Magnetism. 2017; 31(4): 959-979. doi: 10.1007/s10948-017-4245-8

13. Reiss H. Interpretation of experimental critical current density and levitation of superconductors, and a second temperature limit to protect superconductors against quench. ArXiv. 2023.
14. Annett J. Superconductivity, superfluids and condensates. Oxford University Press; 2004.
15. Phelan PE, Flik MI, Tien CL. Radiative properties of superconducting Y-Ba-Cu-O thin films. *Journal of Heat Transfer*. 1991; 113(2): 487-493. doi: 10.1115/1.2910587
16. Falk G, Ruppel W. *Energie und Entropie*. Springer Berlin Heidelberg; 1976. doi: 10.1007/978-3-642-67899-8
17. Kreyszig E. *Statistical methods and their applications (German)*. Vandenhoeck & Ruprecht; 1968.
18. Troitsky OYu, Reiss H. Estimation of thermal diffusivity of thin film materials by a one-level, two-point 'diverging'-thermal-wave technique. Part I: Theory. *High Temperatures-High Pressures*. 2003; 35/36(3): 265-280. doi: 10.1068/htjr100
19. Troitsky OYu, Reiss H. Flash Method for the Remote Sensing of the Thermal Diffusivity and the Absorption Coefficient at the Excitation Wavelength of Thin Film Materials. *International Journal of Thermophysics*. 2007; 28(5): 1536-1541. doi: 10.1007/s10765-007-0231-x
20. Troitsky OYu, Reiss H. A Numerical Simulation to Propose a Flash Method for In Situ Detection of the Thermal Diffusivity of Anisotropic Thin Film Materials. *International Journal of Thermophysics*. 2009; 30(4): 1283-1299. doi: 10.1007/s10765-009-0597-z
21. Reiss H, Troitsky OYu. Radiative transfer and its impact on thermal diffusivity determined in remote sensing. In: Reimer A (editor). *Horizons in World Physics*. Nova Science Publ. Inc; 2012.
22. Troitsky OYu, Reiss H. Radiative transfer and its impact on determination of thermal diffusivity in thin films. *High Temperatures-High Pressures*. 2017; 46: 313-341.
23. Agranat M, Ashitkov S, Kostanovskii A, et al. Thermal radiation and electron - phonon relaxation produced by picosecond laser pulses in metals. *High Temperatures-High Pressures*. 1998; 30(6): 717-721. doi: 10.1068/htec91
24. Siegel R, Howell JR. *Thermal Radiation Heat Transfer*. McGraw- Hill Kogakusha Ltd.; 1972.
25. Parker WJ, Jenkins RJ. Thermal Conductivity Measurements on Bismuth Telluride in the Presence of a 2 MeV Electron Beam. *Adv. Energy Conversion*. 1962; 2: 87-103
26. Chandrasekhar S. *Radiative transfer*. Dover Publ., Inc.; 1960.
27. Whitaker St. *Fundamental principles of heat transfer*. Pergamon Press Inc; 1977
28. Carslaw HS, Jaeger JC. *Conduction of Heat in Solids*, 2nd ed. Oxford Science Publications, Clarendon Press; 1959.
29. Reiss H. The Additive Approximation for Heat Transfer and for Stability Calculations in a Multi-filamentary Superconductor. *Journal of Superconductivity and Novel Magnetism*. 2019.
30. Yuen WW, Wong LW. Heat Transfer by Conduction and Radiation in a One-Dimensional Absorbing, Emitting and Anisotropically-Scattering Medium. *Journal of Heat Transfer*. 1980; 102(2): 303-307. doi: 10.1115/1.3244278
31. Bohren CF, Huffman DR. *Absorption and scattering of light by small particles*. Wiley- Interscience Publ.; 1983.
32. Fitzer G. *Investigation of materials for the development of a superconducting switch (Germany)*. University of Karlsruhe; 1990.
33. Riise AB, Johansen TH, Bratsberg H, et al. Levitation force from high-T_csuperconducting thin-film disks. *Physical Review B*. 1999; 60(13): 9855-9861. doi: 10.1103/physrevb.60.9855
34. Gray KE, Long AR, Adkins CJ. Measurements of the lifetime of excitations in superconducting Aluminium. *Philosophical Magazine*. 1969; 20(164): 273-278. doi: 10.1080/14786436908228699
35. Gray KE. Steady state measurements of the quasiparticle lifetime in superconducting Aluminium. *Journal of Physics F: Metal Physics*. 1971; 1(3): 290-308. doi: 10.1088/0305-4608/1/3/311
36. Mattuck RD. *A guide to Feynman Diagrams in the many-body problem*. MacGraw-Hill Book Company; 1967.

Appendix

Length of the diffusion intervals (τ_{Th} , τ_m , τ_C) is estimated in elementary steps. We have

(i) τ_{Th} of thermal diffusion

This approach applies the relation between position or characteristic dimension, x , and diffusivity, $x = 3.6 (D_{Th} t)^{1/2}$, for a flat sample (this special, “one percent” ($\Theta = 0.01$) relation, is well known, for its derivation see e.g., Whitaker [27], Eq. 4.3–26). It allows to extract diffusion time τ_{Th} that a thermal wave arising from a disturbance at a co-ordinate x' needs to arrive at a position, x , if its diffusivity, D_{Th} , is known.

The thermal diffusivity, D_T , of YBaCuO is between 4×10^{-6} and 2×10^{-6} m²/s, at temperatures of 77 and 120 K, respectively. With $x = 2 \mu\text{m}$ the characteristic dimension (sample thickness in thin films) and D_{Th} of YBaCuO of about 4×10^{-6} m²/s at $T = 90$ K (close enough to $T_{Crit} = 92$ K), the diffusion time (item i) is $\tau_{Th} = 2.8 \cdot 10^{-7}$ s.

(ii) Characteristic (diffusion) time, τ_m , of electrical or magnetic fields and of currents, following Wilson [3] reads $\tau_m \leq 4 r^2 / (\pi^2 D_m)$, using for the diffusivity the expression $D_m = \rho_{NC} / \mu_0$, with ρ_{NC} the specific resistivity of a sample in the normal conducting state and with its characteristic dimension, r . With μ_0 the vacuum constant, we have $D_m = 0.361$ m²/s. This yields $\tau_m \leq 10^{-7}$ s using $r = 2 \mu\text{m}$, as before the thickness of the superconductor layer.

(iii) time τ_C needed to establish new equilibrium charge distributions this period covers total redistribution of electrons and electron pairs in the superconductor, here simulated by exchange of charge between neighboring finite elements in the numerical solution scheme. The estimate, as a diffusion process, following Sect. 7.4 in the study of Wilson [3], yields $\tau_C < 10^{-6}$ s, except for temperatures very close to critical temperature.